# Numerical modeling of wave breaking induced by fixed or moving boundaries

**S. T. Grilli, R. Subramanya**

**Abstract** In this paper, several numerical aspects of an existing model for fully nonlinear waves are improved and validated to study wave breaking due to shoaling over a gentle plane slope and wave breaking induced by a moving lateral boundary.

The model is based on fully nonlinear potential flow theory and combines a higher-order Boundary Element Method (BEM) for solving Laplace's equation at a given time and Lagrangian Taylor expansions for the time updating of the free surface position and potential. An improved numerical treatment of the boundary conditions at the intersection between moving lateral boundaries and the free surface (corner) is implemented and tested in the model, and the free surface interpolation method is also improved to better model highly curved regions of the free surface that occur in breaking waves. Finally, a node regridding technique is introduced to improve the resolution of the solution close to moving boundaries and in breaker jets.

Examples are presented for solitary wave propagation, shoaling, and breaking over a 1:35 slope and for wave breaking induced by a moving vertical boundary. Using the new methods, both resolution and extent of computations are significantly improved compared to the earlier model, for similar computational efforts. In all cases computations can be carried out up to impact of the breaker jets on the free surface.

# 1
## Introduction

Over the past fifteen years, efficient models were developed for the solution of two-dimensional fully nonlinear potential flows with a free surface (FNPF) (e.g., Longuet-Higgins and Cokelet (1976) (LHC); Vinje and Brevig (1981); New, McIver and Peregrine (1985); Dold and Peregrine (1986) (DP); Grilli, Skourup, and Svendsen (1989) (GSS)). A few attempts have also been reported in solving FNPF problems in three dimensions (Romate (1989) (ROM); Xü and Yue (1992); Broeze (1993))

S. T. Grilli, R. Subramanya
Ocean Engineering Department, University of Rhode Island, Narragansett, RI 02882, USA

Correspondence to: St. T. Grilli

(see also the reviews in (GSS; ROM). In most successful approaches, Laplace's equation is solved at a given time based on a Boundary Integral Equation (BIE) or on a Boundary Element Method (BEM), and free surface geometry and potential are updated in time based on a mixed Eulerian-Lagrangian description of the free surface.

In the earlier models, waves were assumed to be periodic in space and the problem was then solved in a transformed space and/or using a complex variable formulation (e.g., LHC; DP). To apply the method to arbitrary waves, complex bottom topography, or moving boundaries, other models were proposed which solved the equations directly in the physical space (Lin, New and Newman (1984) (LNN); GSS; Cointe (1990)). [Note also that, for cases in which the unsteady flow vanishes in both horizontal directions, Cooker (1990) extended the space periodic model by DP to irregular bottom topography.] These models, however, sometimes had problems when simulating the generation of waves by wavemakers (e.g., LNN). Among these early models, the model by GSS and Grilli and Svendsen (1990) (GS), was the object of considerable developments and improvements which made it particularly versatile and accurate for solving problems of wave breaking induced by fixed or moving boundaries. In this model, Laplace's equation is solved by a higher-order BEM based on 2nd Green's identity (a method also applicable to three-dimensional problems unlike earlier approaches based on complex variables), using isoparametric elements for the spatial discretization (2nd to 4th-order), and time integration is explicit and based, as in DP, on (2nd-order) truncated Taylor series expansions. More details about this numerical model can also be found in Grilli (1993).

When working in the physical space, incident waves must be generated and reflected or absorbed in the model, which poses much more difficult problems than with space-periodic models. The modeling of wave absorption using a "sponge layer" is discussed, e.g., in Cointe (1990) and Grilli and Horrillo (1995) (see Otta, Svendsen and Grilli (1992) (OSG) for a literature review). The modeling of the intersection – or corner – between the free surface and a fixed or a moving boundary has been the object of a substantial amount of work in the literature, in the context of wave generation by a wavemaker starting from a state of rest (Roberts (1987); Cointe (1989); GS (also for a literature survey to date); Joo, Schultz and Messiter (1990); OSG; Svendsen, Otta and Grilli (1992)). It was thus found that the sudden jump to a finite value of the wavemaker initial velocity and acceleration may create an initial (mathematical) singularity of the flow near the wavemaker. This singularity results from inconsistencies between boundary conditions on the free surface and on the wavemaker and, if

not properly accounted for in the numerical model, invariably worsens through time marching, eventually leading to instability of the numerical solution. Such a problem may be addressed two ways in a numerical model: (i) either by explicitly introducing the singular behavior of the flow in the numerical solution (as, e.g., discussed in Cointe (1988)); (ii) or, more simply, by specifying initial boundary conditions in such a way that both inconsistencies and singularities do not occur (OSG). The latter method is further discussed in the paper and will be used in the present applications.

Besides the possible occurrence of an initial (mathematical) singularity of the solution, it can been seen that additional problems – most of these being generic to BEM/BIE methods – can occur at corners as a result of improper numerical representation of the solution. In fact, without special treatments of corners, BEM/BIE solutions usually exhibit large errors at corners, even when the actual mathematical solution is non-singular (e.g., Schultz and Hong (1989)). In the context of wave generation by wavemakers, a poor numerical solution at corners may thus have all the appearances of singular behavior and, through time marching, lead to instability of the numerical solution. GSS and GS analyzed the causes for such (numerical) singularity problems and proposed specific numerical treatments to eliminate them: (i) the representation of corners by double-nodes and the use of continuity conditions for the potential; (ii) the specification of fluid velocity uniqueness at corners through using compatibility conditions between the normal and tangential derivatives of the potential; (iii) the improved accuracy of (non-singular but potentially quasi-singular) numerical integrations at corners, through using adaptive numerical integration techniques. Using such treatments, GS calculated the solution of various mixed boundary value problems, in computational domains with sharp corners, with almost arbitrarily small errors and GS; Svendsen and Grilli (1990); Grilli, Losada and Martin (1994); Grilli, Subramanya and Svendsen (1994), successfully computed wave generation by a wavemaker and wave propagation and runup over slopes and over other bottom discontinuities or structures. Finally, based on the same methods as in GS, OSG developed extended corner compatibility conditions (numerical treatment (ii)) which provided further improvements of the corner solution in the case of wavemaker motion. These extended conditions are detailed in the present paper and will be tested in the applications versus the earlier approaches by GSS and GS.

In the model by GSS and GS, as in most earlier models based on a mixed Eulerian-Lagrangian description, free surface discretization nodes represent water particles whose position is calculated as a function of time. Doing so, multiple-valued free surface elevations can be represented and overturning waves can in principle be calculated up to the time the tip of the breaker jet impacts the free surface (thus violating continuity equation and leading to numerical instability of the computations). This is illustrated in the applications in this paper. It is worth pointing out that laboratory experiments and computations by Dommermuth, Yue, Lin, Rapp, Chan and Melville (1988), for deep water breakers, and by Grilli, Subramanya, Svendsen and Veeramony (1994) (GSSV), for shallow water breakers, both confirmed the physical validity of the FNPF results up to the point of impact (see also results by Grilli, Svendsen and Subramanya (1994)).

In using the model by GSS to compute overturning waves, GS reported numerical inaccuracies of the solution in highly curved regions of the free surface, like breaker jets, before wave overturning could be fully calculated. They showed that these inaccuracies were due to small discontinuities in the free surface slope occurring between successive isoparametric elements and could be eliminated with a representation of the free surface geometry ensuring continuity of the slope. This representation used linear shape functions to discretize field variables and cubic splines to represent the geometry, and was referred to as "quasi-spline boundary elements" (QS). Despite the linear shape functions, QS elements proved quite accurate for a wide range of applications of the model (e.g., Grilli (1993); Grilli, Losada and Martin (1994)). A more detailed analysis of this problem by OSG also showed that, when using higher-order isoparametric elements on the free surface – and not linear elements as in most earlier models (e.g., LHC; VB) – due to the shape function representation of the geometry, time updating of intermediate nodes in the elements is treated slightly differently than time updating of extremity nodes. Such differences in the updating may make small discontinuities in inter-element slope grow with time, particularly in regions of high curvature, and trigger larger scale instabilities of the free surface. In fact, using simpler piecewise linear elements on the free surface, which do not have intermediate nodes, GSS were able to compute large scale plunging breakers identical to those reported in (LHC; VB; NMP) without facing instability problems discussed above. Overall, however, their solution was less accurate than when using higher-order elements that do not have discontinuity of the slope (see below). This is because a higher-order representation of the free surface improves both the accuracy and the convergence of the BEM solution of Laplace's equation (GSS; OSG). OSG thus introduced a higher-order representation of the free surface for both the geometry and the field variables that ensures continuity of the free surface slope. To do so, they defined the interpolation within each free surface segment between two nodes using the middle interval of a four-node cubic isoparametric element (thereafter referred to as "mid-interval interpolation" or MII)[1]. In the computations, the MII element is slid along the free surface, one node at a time, thus defining a full cubic interpolation (unlike with the QS elements) with a continuous slope. Using the MII method, OSG showed improvements of several orders of magnitudes in computational accuracy, as compared to the QS method, without significant change in computing time. Although the MII method proved very accurate for the solution of problems with fixed boundaries, it was found less accurate or even unstable for problems with strong interactions between a moving lateral boundary and the free surface. In this paper, it is shown that results can be improved for such cases using a modified MII method in which a cubic spline is used for the interpolation of the geometry and the same sliding cubic polynomial as in the MII method is used for the interpolation of the field variables. This new interpolation method, thereafter referred to as "mixed cubic interpolation" or MCI, is detailed in the paper and computational examples are presented for wave breaking induced by fixed or moving boundaries.

375

---

[1] This, in fact, followed the same principle as used in DP for space-periodic problems.

Finally, when generating waves by a moving boundary (wavemaker), it is observed that free surface nodes gradually drift away from the moving boundary and concentrate in convergence regions of the flow like breaker jets (e.g., GSS). This node drift is due to the mean nonlinear mass flux of the flow – the so-called Stokes drift – and is predicted by nonlinear wave theories. In the present case, with time, node drift leads to a poor resolution of the discretization close to the wavemaker, a region of the flow with large variations of field variables requiring good resolution of the discretization, and to a high concentration of nodes in breaker regions, which may create quasi-singular situations. Both of these node drift effects result in increased computational errors, which are discussed in the paper, and an adaptive regridding technique is introduced to redistribute nodes along a numerically calculated free surface and improve the accuracy of computations in such situations[2].

## 2
## The mathematical and numerical model

### 2.1
### Governing equations and boundary conditions

Equations for the two-dimensional potential model by (GSS; GS) are briefly listed in the following. The velocity potential $\phi(x,t)$ is used to represent inviscid irrotational 2D flows in the vertical plane $(x,z)$ and the velocity is defined by, $u = \nabla\phi = (u,w)$ (Fig. 1). Continuity equation in the fluid domain $\Omega(t)$ with boundary $\Gamma(t)$ is a Laplace's equation for the potential,

$$\nabla^2\phi = 0 \quad \text{in} \quad \Omega(t) \tag{1}$$

Using the free space Green's function, $G(x,x_l) = -(1/2\pi) \log|x - x_l|$, and Green's second identity, Eq. (1) transforms into the Boundary Integral Equation (BIE),

$$\alpha(x_l)\phi(x_l) = \int\limits_{\Gamma(x)} \left[ \frac{\partial\phi}{\partial n}(x) G(x,x_l) - \phi(x) \frac{\partial G(x,x_l)}{\partial n} \right] d\Gamma(x) \tag{2}$$

in which $x = (x,z)$ and $x_l = (x_l,z_l)$ are position vectors for points on the boundary, $n$ is the unit outward normal vector, and $\alpha(x_l)$ is a geometric coefficient function of the exterior angle of the boundary at $x_l$.

On the free surface $\Gamma_f(t)$, $\phi$ satisfies the nonlinear kinematic and dynamic boundary conditions,

$$\frac{Dr}{Dt} = u = \nabla\phi \qquad \text{on} \; \Gamma_f(t) \tag{3}$$

$$\frac{D\phi}{Dt} = -gz + \frac{1}{2}\nabla\phi \cdot \nabla\phi - \frac{p_a}{\rho} \qquad \text{on} \; \Gamma_f(t) \tag{4}$$

respectively, with $r$ the position vector of a free surface fluid particle, $g$ the acceleration due to gravity, $z$ the vertical coordinate (positive upwards, and $z = 0$ at the undisturbed free surface), $p_a$ the atmospheric pressure, $\rho$ the fluid density,

and the material derivative being defined as,

$$\frac{D}{Dt} \equiv \frac{\partial}{\partial t} + u \cdot \nabla \tag{5}$$

Waves can be generated by simulating a piston wavemaker motion on the "open sea" boundary of the computational domain, $\Gamma_{r1}(t)$. In this case, wavemaker motion and velocity $[x_p, u_p]$ are specified over the wavemaker paddle as,

$$\bar{x} = x_p; \quad \nabla\phi \cdot n \equiv \overline{\frac{\partial\phi}{\partial n}} = -u_p \quad \text{on} \; \Gamma_{r1}(t) \tag{6}$$

where overlines denote specified values (see GS for detail).

Along the stationary bottom $\Gamma_b$, and on other fixed boundaries $\Gamma_{r2}$, a no-flow condition is prescribed as,

$$\overline{\frac{\partial\phi}{\partial n}} = 0 \quad \text{on} \; \Gamma_b \; \text{and} \; \Gamma_{r2} \tag{7}$$

### 2.2
### Boundary discretization

The BIE (2) for $(\phi, \partial\phi/\partial n)$ is solved by a Boundary Element Method (BEM, Brebbia (1978)) using a set of $N_\Gamma$ collocation nodes on the boundary and $M_\Gamma = M + M_f$ higher-order elements to interpolate in between the collocation nodes (with $M_f$, the number of elements on the free surface, and $M$, the number of elements on the rest of the boundary). In these boundary elements, both the boundary geometry and the field variables $(\phi, \partial\phi/\partial n)$ are interpolated based on nodal values and on polynomial shape functions and/or on cubic splines.

Integrals in (2) are transformed into a sum of integrals over the elements which are numerically calculated within a single reference element $\Gamma_\xi$, with intrinsic coordinate, $\xi \in [-1, +1]$. A curvilinear change of variable is defined to map each element of boundary segment $\Gamma_\xi^k$ onto the reference element. We hence obtain the following discretized forms for the integrals,

$$\int\limits_{\Gamma(x)} \frac{\partial\phi}{\partial n}(x) G(x,x_l) d\Gamma(x) = \sum_{j=1}^{N_\Gamma} \left\{ \sum_{k=1}^{M+M_f} \int_{\Gamma_\xi} N_j(\xi) G(x(\xi),x_l) \right.$$

$$\left. \frac{\partial s^k}{\partial \xi}(\xi) d\xi \right\} \frac{\partial\phi}{\partial n}(x_j) = \sum_{j=1}^{N_\Gamma} \left\{ \sum_{k=1}^{M+M_f} I_{d_{lj}}^k \right\} \frac{\partial\phi_j}{\partial n} = \sum_{j=1}^{N_\Gamma} K_{d_{lj}} \frac{\partial\phi_j}{\partial n} \tag{8}$$

$$\int\limits_{\Gamma(x)} \phi(x) \frac{\partial G(x,x_l)}{\partial n} d\Gamma(x) = \sum_{j=1}^{N_\Gamma} \left\{ \sum_{k=1}^{M+M_f} \int_{\Gamma_\xi} N_j(\xi) \frac{\partial G(x(\xi),x_l)}{\partial n} \right.$$

$$\left. \frac{\partial s^k}{\partial \xi}(\xi) d\xi \right\} \phi(x_j) = \sum_{j=1}^{N_\Gamma} \left\{ \sum_{k=1}^{M+M_f} I_{n_{lj}}^k \right\} \phi_j = \sum_{j=1}^{N_\Gamma} K_{n_{lj}} \phi_j \tag{9}$$

in which, $l = 1,...,N_\Gamma; j$ denotes nodal values with $N_j(\xi)$ the reference element shape function at node $j$; and $\partial s^k/\partial\xi$ is the Jacobian of the transformation for the $k$-th boundary element.

Using (8), (9), the discretized form of the BIE (2) reads,

$$\alpha_l \phi_l = \sum_{j=1}^{N_\Gamma} \left\{ K_{d_{lj}} \frac{\partial\phi_j}{\partial n} - K_{n_{lj}} \phi_j \right\} \tag{10}$$

---

[2] Note that such a redistribution of nodes does not constitute smoothing (as, e.g., used in LHC).

in which, $l = 1,...,N_\Gamma$. Boundary conditions are introduced in (10) for $\phi$ (see time stepping section) and for $\partial\phi/\partial n$ (see Eqs. (6), (7)), and the final algebraic system is assembled by moving unknowns to the left hand side and keeping specified terms in the right hand side. The solution of this system is simply calculated using Kaletsky's LU elimination method. Note that coefficients $\alpha_l$ are computed together with the diagonal coefficients of $K_{n_{ij}}$ using the "rigid mode" method (Brebbia (1978)). This method has been shown to improve both the conditioning and the accuracy of the solution of the resulting algebraic system (GSS).

Expressions for both the shape functions and the Jacobian in (8), (9) are given in GSS for isoparametric elements. In the applications, these will be used for the discretization on lateral boundaries $\Gamma_{r1}$, $\Gamma_{r2}$, and on the bottom $\Gamma_b$ (Fig. 1). Expressions for both the shape functions and the Jacobian on the free surface $\Gamma_f$ are detailed in the following for three different interpolation methods (QS, MII, and MCI).

### 2.1.1
### Quasi-Spline elements (QS)

As discussed in the introduction, QS elements were introduced in GS to improve the accuracy of computations in highly curved regions of the free surface. In the QS elements, shape functions are linear polynomials in $\zeta$ and the geometry is modeled by cubic splines (ensuring continuity of the inter-element slope). To represent multiple-valued free surface elevations occurring in overturning waves, the geometry is defined based on two standard single-valued spline approximations, for $[x(\tau_j), \tau_j]$ and $[z(\tau_j), \tau_j]$, in which $\tau$ denotes the node index,

$$\tau(x_j) = \tau_j = 1,...,N_f \quad \text{and} \quad \zeta(\tau) = 2(\tau - \tau_j) - 1 \qquad (11)$$

with $N_f$ the number of nodes on the free surface.

For the $k$-th QS element, geometry, $x^k(\tau) = (x^k(\tau), z^k(\tau))$, is thus defined as,

$$x^k(\tau) = (k + 1 - \tau)x_k + (\tau - k)x_{k+1} + \frac{A(\tau)}{6}(A^2(\tau) - 1)\frac{d^2x_k}{d\tau^2}$$

$$+ \frac{B(\tau)}{6}(B^2(\tau) - 1)\frac{d^2x_{k+1}}{d\tau^2} \qquad (12)$$

$$A(\tau) = k + 1 - \tau; \quad B(\tau) = \tau - k; \quad \tau(\xi) = k + \frac{\xi + 1}{2} \qquad (13)$$

in which $\tau_j = k$ for element $\Gamma_e^k(k = 1,...,M_f)$, $(x_k, x_{k+1})$ denote element $k$ nodal coordinates, and second-order derivatives of
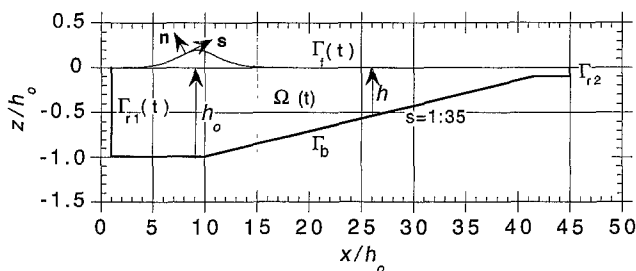




**Fig. 1.** Sketch of typical computational domain for solitary wave shoaling over a gentle 1:35 slope

these are obtained from the spline analyses. End node slopes, $dx/d\tau$ and $dz/d\tau$, required as boundary conditions in the spline analyses, are in general specified for both extremities on the free surface based on 4-node cubic polynomial approximations. In some specific cases, however, the slope at one extremity of the free surface can be obtained from the physics of the problem (e.g., zero slope at a vertical wall) and hence can be explicitly specified as a boundary condition in the spline analyses.

The Jacobian of the transformation from the $k$-th free surface element to the reference element is defined, using (11) as,

$$\frac{\partial s^k}{\partial \xi}(\xi) = \frac{\partial s^k}{\partial \tau}(\xi)\frac{\partial \tau}{\partial \xi}(\xi) \qquad (14)$$

or,

$$\frac{\partial s^k}{\partial \xi}(\xi) = \frac{1}{2}\left[\left(\frac{dx^k}{d\tau}(\tau(\xi))\right)^2 + \left(\frac{dz^k}{d\tau}(\tau(\xi))\right)^2\right]^{1/2} \qquad (15)$$

which can be calculated using (12), (13). The outward unit normal vector along the $k$-th element is similarly obtained as,

$$n^k(\xi) = \frac{1}{2}\left[-\frac{dz^k}{d\tau}(\tau(\xi)), \frac{dx^k}{d\tau}(\tau(\xi))\right]\bigg/\frac{\partial s^k}{\partial \xi} \qquad (16)$$

### 2.1.2
### Cubic Mid-Interval Interpolation method (MII)

OSG developed a full cubic interpolation method, the MII method, in which both geometry and field variables are approximated between each pair of nodes $(k, k + 1)$ on the free surface – except for the first and last pairs including corners – using the mid-section of a cubic (four-node) "sliding" isoparametric element. At both extremities on the free surface, the first two nodes and the last two nodes of the sliding element are used for the interpolation in between the first and last pairs of nodes, respectively. After each interpolation, the four-node element is "slid" forward along the free surface, which ensures local continuity of the inter-element slope.

Shape functions, to be used in (8), (9), are cubic polynomials defined in the sliding element of intrinsic coordinate $\mu$ by,

$$N_j(\mu_i) = \delta_{ij} \quad \text{with} \quad \mu_i = (2i - 5)/3 \qquad (17)$$

in which $\delta_{ij}$ is the Kronecker's symbol; $i, j = 1,...,4$; and $\mu_i$ are intrinsic nodal coordinates for the sliding element. Hence,

$$N_1(\mu) = \frac{1}{16}(1 - \mu)(9\mu^2 - 1); N_2(\mu) = \frac{9}{16}(1 - \mu^2)(1 - 3\mu)$$

$$N_3(\mu) = \frac{9}{16}(1 - \mu^2)(1 + 3\mu); N_4(\mu) = \frac{1}{16}(1 + \mu)(9\mu^2 - 1) \quad (18)$$

The mid-interval segment of the sliding element is mapped onto the usual reference element $\Gamma_\xi$ by,

$$\mu(\xi) = \mu_l + (\mu_r - \mu_l)\frac{1 + \xi}{2} \qquad (19)$$

in which $(\mu_l, \mu_r)$ denote intrinsic coordinates for the leftward and rightward nodes of the MII interval, i.e., by (17): $(-\frac{1}{3}, +\frac{1}{3})$ for the mid-interval, and $(-1, -\frac{1}{3})$ or $(+\frac{1}{3}, +1)$ for the leftward and rightward extremities.

The Jacobian of the transformation from the $k$-th free surface element (i.e., segment $(k, k+1)$) to the reference element is,

$$\frac{\partial s^k}{\partial \xi}(\xi) = \frac{d\mu}{d\xi}\left[\left(\frac{dx^k}{d\mu}(\mu(\xi))\right)^2 + \left(\frac{dz^k}{d\mu}(\mu(\xi))\right)^2\right]^{1/2} \quad (20)$$

where, using (19), $d\mu/d\xi = (\mu_r - \mu_l)/2 = 1/3$, and,

$$x^k(\mu) = \sum_{j=1}^{4} x_j^k N_j(\mu) \quad \text{and} \quad \frac{dx^k}{d\mu}(\mu) = \sum_{j=1}^{4} x_j^k N_j'(\mu) \quad (21)$$

in which $(x_j^k, j = 1,...,4)$ denote coordinates for the nodes of the sliding element centered on free surface segment $k$, and $N_j'(\mu)$ are derivatives of shape functions (18).

### 2.1.3
### Mixed Cubic Interpolation method (MCI)

In the present paper, the QS and the MII methods are combined into the "Mixed Cubic Interpolation method" (MCI) for which field variables are interpolated, as in the MII method, using the mid-section of a cubic "sliding" isoparametric element and the geometry is modeled, as in the QS method, using two cubic spline approximations, for $[x(\tau_j), \tau_j]$ and $[z(\tau_j), \tau_j]$ $(j = 1,...,N_f)$. In the MCI method, Eqs. (11) to (16) are thus used for the modeling of free surface geometry and shape functions $N_j(\mu(\xi))$, defined by (17) to (19), are used for interpolating the field variables.

Both the accuracy of the MCI method and reasons for introducing this method will be discussed in the applications.

### 2.3
### Numerical integrations

Non-singular integrals in (8), (9) ($I_{d_{ij}}^k$ and $I_{n_{ij}}^k$ for $l \neq j$) are calculated over each element $k$ using a standard Gauss quadrature, usually with ten integration points in order to obtain sufficient accuracy for higher-order elements, in domains with large aspect ratios (e.g., GS). Integrals with a weak logarithmic singularity ($I_{d_{ij}}^k$ for $l = j$) are first transformed into a standard form by isolating the singular kernel which is then integrated using a numerical quadrature exact for the logarithmic singularity (GSS). Strong singularities in the integrals ($I_{n_{ij}}^k$ for $l = j$) are removed during the derivation of the BIE (2), to constitute part of the values of coefficients $\alpha(x_l)$. Although non-singular, resulting integrals may still have a highly varying kernel when distance $|x - x_l|$ gets small. Accuracy of these integrals is improved by first performing an integration by parts and then using a standard Gauss quadrature rule to evaluate the remaining integral (GSS).

Quasi-singular integrals may occur near corners and in other regions of the free surface, like overturning breaker jets, where nodes are close to elements on different parts of the boundary. Although non-singular, these integrals, due to the short distance from, say, collocation node $x_l$ to the boundary, have a highly varying kernel that a standard Gauss quadrature rule fails to accurately integrate unless a prohibitive number of integration points is used (GS). Grilli and Subramanya

(1994) showed that the loss of accuracy of Gauss integrations (with ten integration points) for such quasi-singular integrals may be of several orders of magnitudes when the distance to the collocation node becomes very small. GS developed an adaptive integration scheme based on a binary subdivision of the reference element and obtained almost arbitrary accuracy for the quasi-singular integrals, when increasing the number of subdivisions. This method, however, can be computationally expensive and Grilli and Subramanya (1994) developed a more efficient method that essentially redistributes integration points around the location of the quasi-singularity (point of minimum distance from an element $k$ to the nearest collocation node, $x_l$). The latter method will be used in the present applications for calculating quasi-singular integrals.

### 2.4
### Node regridding

As discussed in the introduction, free surface discretization nodes represent fluid particles and, hence, drift in the direction of the mean mass flux of the flow, thereby affecting resolution of the discretization. To either add and redistribute nodes in regions of poor resolution of the free surface or to remove and redistribute nodes in regions of node concentration, a regridding technique is implemented in the model in combination with the MCI interpolation method. This technique redistributes nodes within a specified boundary section based on a constant arc length interval. Field variables are then re-interpolated at the new locations of nodes in the section.

More specifically, a node arc length vector, $s_l$ (with $l = 1,...,N_f$) is first calculated for the old locations of nodes, $x_l$, by computing, $\int_0^{s(x_l)} ds$, over the entire free surface as a summation over free surface elements. A boundary section is then defined over which regridding is to be performed and the (arbitrary) number of nodes to be added to or removed from this section is used for computing the new arc length increment within the section. Based on this increment, a new arc length vector, $s_l^r$, is calculated for regridded nodes and mapped node by node onto $s_l$ to isolate element $k$ (old nodes $(k, k+1)$) within which new nodes are located. For each such element, an iterative procedure is used to calculate the intrinsic coordinate $\xi$ corresponding to a given component of $s_l^r$ and, based on this, nodal coordinates $x_l = x^k(\xi)$ are re-calculated for the new node locations, using (12) and (13) for the MCI method, and similarly for the field variables, using the element shape functions (18) with (19).

Computations are pursued as before in the regridded discretization. We will see, however, that the optimal size of the time step in the time updating part of the model is function of the minimum distance between free surface nodes. Since regridding changes this distance, adjustments must also be made to the time step in order for the computations to stay accurate and stable. This will be discussed in the applications.

As mentioned above, discretization nodes gather in regions of flow convergence. When nodes are added to a free surface section and regridded, the mean distance between nodes in this section is decreased and quasi-singular situations are likely to occur even more often than prior to regridding. To prevent free surface nodes from getting too close to each other (in fact, with or without regridding) and to limit the

occurrence of such quasi-singularities, an adaptive regridding procedure is implemented in the model. When the distance between two nodes becomes 50% smaller (or larger) than the distance between neighboring nodes, nodes are locally regridded to make these distances identical. This procedure will also be discussed and used in the applications.

## 2.5
## Time stepping and global accuracy

Free surface boundary conditions (3) and (4) are integrated at time $t$ to establish both the new position and the boundary conditions on the free surface at subsequent time $(t + \Delta t)$ (with $\Delta t$ the time step). Second-order Taylor series expansions are used to express both the new position $r(t + \Delta t)$ and the potential $\phi(r(t + \Delta t))$ on the free surface, in an Eulerian-Lagrangian formulation based on the material derivative (5),

$$\bar{r}(t + \Delta t) = r(t) + \Delta t \frac{Dr}{Dt}(t) + \frac{(\Delta t)^2}{2} \frac{D^2 r}{Dt^2}(t) + \mathcal{O}[(\Delta t)^3] \quad (22)$$

$$\bar{\phi}(r(t + \Delta t), t + \Delta t) = \phi(t) + \Delta t \frac{D\phi}{Dt}(t)$$

$$+ \frac{(\Delta t)^2}{2} \frac{D^2 \phi}{Dt^2}(t) + \mathcal{O}[(\Delta t)^3] \quad (23)$$

Coefficients in the Taylor series are expressed as functions of the potential, its time derivative, and the normal and tangential derivatives of both of these along the free surface (GSS; Grilli (1993)). This method has the advantages, compared to Runge-Kutta (RK) and Adams-Bashforth-Moulton (ABM) time stepping schemes used in earlier models (LHC; VB; NMP), of both being explicit and accounting for spatial derivatives along the free surface ($\partial/\partial s$, $\partial^2/\partial s^2$) in the calculation of values at $(t + \Delta t)$. This provides a better stability of the computed solution and makes it possible to use larger time steps, for a similar accuracy, thus also making the overall solution more efficient (see also discussions in RO, OSG).

To calculate coefficients in series (22), (23), normal and temporal derivatives of the potential are obtained from the solution of two BIE's of the form (2), for $(\phi, \partial\phi/\partial n)$ and $(\partial\phi/\partial t, \partial^2\phi/\partial t\partial n)$, and tangential derivatives are computed using a five-node 4th-order "sliding" element, independent from the BEM discretization. Boundary conditions for the second BIE for $\partial\phi/\partial t$ are obtained from the solution of the first BIE for $\phi$. Note that both BIE's correspond to the same boundary geometry and, hence, have the same discretized form (10). Therefore, the solution of the second BIE only takes a small fraction of the time (typically a few percent) needed for the solution of the first BIE which, again, makes the present time stepping method very efficient, particularly, compared to higher-order RK or ABM schemes which often require multiple evaluations of the BIE (2) for several intermediate times per time step.

In the applications, global accuracy of the computations is checked at each time step by computing errors in total volume $m$ and energy $e$ for the generated wave train. Numerical errors are function of the size (i.e., distance between nodes) and degree (i.e., quadratic, cubic,...) of the boundary elements

used in the spatial discretization, both of which control the accuracy of the BEM solution of Laplace's equation, and of the size of the selected time step, which controls the accuracy of the time stepping. GS developed a criterion for selecting the optimum time step size in the model based on results of computations made in various spatio-temporal discretizations for the propagation over a given time (i.e., distance) of a large solitary wave. Using QS elements on the free surface and quadratic isoparametric elements elsewhere on the boundary, they showed that, for a constant time step $\Delta t_o$, errors in $m$ and $e$ reach a minimum when the mesh Courant number,

$\mathcal{C}_o = \sqrt{gh} \Delta t_o / \Delta x_o \simeq 0.5$ (in which $\Delta x_o$ denotes the initial distance between nodes on the free surface and $h$ the characteristic depth). Thus, despite more accurate results in the time updating (22), (23) when a smaller time step is used (truncation errors are $\mathcal{O}[(\Delta t_o)^3]$), the model may provide larger overall errors, in a given initial discretization, when the time step is too small. The reason for this is that, for very small time steps, too many computational steps are needed for the wave to cover the specified time (or distance) of propagation in the model, which leads to an "accumulation" of numerical errors (i.e., truncation, round-off) resulting from the solution of Laplace's equation. Hence, in such cases, overall accuracy can only be improved by reducing $\Delta x_o$, thus making the solution of Laplace's equation more accurate, and achieving optimum $\mathcal{C}_o$.

Based on these results, GS proposed an adaptive time step method applicable to highly transient waves – like breakers – for which the distance between nodes widely varies. In this method, time step $\Delta t$ is adaptively calculated as a function of time $t$ based on the optimum mesh Courant number, $\mathcal{C}_o$, and on the instantaneous minimum distance between nodes on the free surface, $\Delta|r(t)|^{min}$,

$$\Delta t = \mathcal{C}_o \frac{\Delta|r|^{min}}{\sqrt{gh}} \quad (24)$$

Similar calculations will be presented in the first application in this paper, using the MII or the MCI method for the interpolation on the free surface, in order to determine the corresponding optimum value of $\mathcal{C}_o$, if any.

## 2.6
## Discretized boundary conditions at corners

In the following, we assume that initial boundary conditions are selected in the model in such a way that the flow at corners does not have an initial (mathematical) singularity (see Sect. 3.3 for details). As discussed in the introduction, well-posed discretized boundary conditions must be specified at corners to avoid occurrence of numerical singularities during the course of computations[3].

Boundary conditions and normal directions are in general different for each side of corners in the computational domain

---

[3] Gray and Lutz (1990) and Gray and Manne (1993) showed that, provided the discretization of field variables on both sides of a corner is consistent, terms which are potentially singular at corners will cancel. In turn, ill-posedness of corner boundary conditions through inconsistent discretization will create the equivalent of hypersingularities.

(e.g., on a wavemaker and on the free surface; see Fig. 1). To be able to specify such differences, corners are represented by double-nodes for which coordinates are identical but normal vectors are different (GSS; GS). Thus, two different discretized BIE's (Eq. (10)) are expressed for each node of a corner double-node, say: (i) for $l = p$, on the wavemaker paddle; and (ii) for $l = f$, on the free surface. Since potential must be unique at a given location, however, one of these two BIE's must be modified in the final discretized system to explicitly satisfy, $\phi_p = \phi_f$ (i.e., "continuity of the potential", GS).

380

In addition, for free surface corners, the velocity vector must also be unique, i.e. $u_p = u_f$, for both corner (double) nodes to move to identical locations through time updating. GS and OSG showed that, if this "velocity continuity" is not explicitly specified in the discretized BIE system (10), large numerical errors will occur at corners which will grow even larger through time stepping and, eventually, will lead to instability of the solution, particularly close to a strongly moving lateral boundary[4]. Hence, they derived discretized relationships expressing velocity uniqueness (compatibility) at corners for all cases of mixed Dirichlet-Neuman boundary conditions. These relationships, in fact, make the representation of the solution compatible (i.e., consistent on both sides of a corner in the sense of the study by Gray and Lutz (1990) and effectively eliminate (numerical) singularities in the discretized solution.

When using compatibility conditions at corners for solving mixed boundary value problems in simple rectangular domains, GS showed that numerical errors at corners could be reduced to almost arbitrarily small values. At the intersection between a piston wavemaker and the free surface, for instance, they used a velocity compatibility condition to specify a (corrected) value of the tangential velocity, $\partial\phi_f/\partial s$, as a function of both the normal velocity, $\partial\phi_f/\partial n$, obtained from the solution of the BIE (10) at each time step, and the (known) wavemaker velocity, $\overline{\partial\phi_p/\partial n} = -u_p(t)$ (see (6)), before calculating time updating of the free surface. This condition reads,

$$\frac{\partial\phi_f}{\partial s} = \frac{\partial\phi_f}{\partial n}\tan\beta_f - \overline{\frac{\partial\phi_p}{\partial n}}\sec\beta_f \qquad (25)$$

in which $\beta_f$ is the angle between the free surface and the horizontal. The velocity obtained in (25) is thus used in replacement of the tangential velocity otherwise calculated in the 4th-order sliding polynomial, to make velocity components a posteriori compatible for both sides of the corner.

By performing additional numerical tests, OSG showed that using (25) a posteriori may not be accurate enough for strongly moving lateral boundaries. Hence, they further developed this equation to a priori specify velocity compatibility at each time step within the discretized BIE system (10), before the solution is calculated. To do so, they first expressed the tangential velocity in (25) as a linear combination of nodal values of the potential within a 4th-order sliding element

located over the first five nodes of the free surface ($k = 1$),

$$\frac{\partial\phi_f}{\partial s} = \left\{\sum_{j=1}^{5} N_j'(\mu_1)\phi_j\right\}\bigg/\frac{\partial s^k}{\partial\xi}(\mu_1) = \sum_{j=1}^{5}\mathscr{F}_j\phi_j \qquad (26)$$

in which, by (17), $\mu_1 = -1$ for the first node in the element, and $N_j'(\mu)$ denote first derivatives of the sliding element quartic shape functions, obtained by (17) with $i, j = 5$. Combining (25) and (26), they finally expressed the corner compatibility equation as,

$$\mathscr{F}_1\phi_p - \frac{\partial\phi_f}{\partial n}\tan\beta_f = u_p\sec\beta_f - \sum_{j=2}^{5}\mathscr{F}_j\bar{\phi}_j \qquad (27)$$

in which $\phi_1 = \phi_f = \phi_p$, and the last term in the right hand side is a linear combination of values of the free surface potential specified using time updating Eq. (23). Equation (27) is introduced in line $l = p$ of the discretized system (10), in replacement of the BIE for the wavemaker side of the corner, and the other corner equation in line $l = f$ of the system is, as before, the discretized BIE for the free surface side of the corner. Although prescribed on the free surface by the time updating (23), the potential in the corner, $\phi_p = \phi_f$, is now considered as an unknown to be calculated as part of the system solution in order to satisfy velocity compatibility. Hence, coefficients of $\phi_p$ and $\phi_f$ are lumped together for lines $l \neq p$ of the system (10).

Compatibility equations similar to (27) are also expressed for $\partial\phi/\partial t$ and for all the other cases of mixed boundary conditions at corners (Dirichlet and Neuman types) discussed by GS. OSG showed that using equations such as (27) at corners significantly improves both the accuracy and the stability of the numerical solution, particularly for cases of waves generated by wavemakers. These new extended compatibility conditions have been implemented in the present model and their accuracy is compared to the old corner compatibility conditions (type (25)), in the last application in the next section.

## 3
## Applications

### 3.1
### Global accuracy for solitary wave propagation over constant depth

Computations are carried out as in GS to determine the optimal mesh Courant number $\mathscr{C}_o$ corresponding to minimum numerical errors for given discretizations and interpolation methods on the free surface. Numerically exact solitary waves obtained using the fully nonlinear method by Tanaka (1986) are used as incident waves (see GS for detail) and are propagated over constant depth $h$ in various spatio-temporal discretizations (Fig. 2). Such solitary waves should keep permanent form, constant volume and total energy while propagating in the model. Computational errors with respect to Tanaka's results for each wave thus give a measure of discretization and time step effects on global numerical accuracy, for different interpolation methods used in the free surface.

Solitary waves of height $H/h = 0.3$ to $0.6$ are used in the computations and computational data are identical to those for the same applications in GS. The domain aspect ratio is

---

[4] This is also consistent with the conclusions in Gray and Lutz (1990) and Gray and Manne (1993).
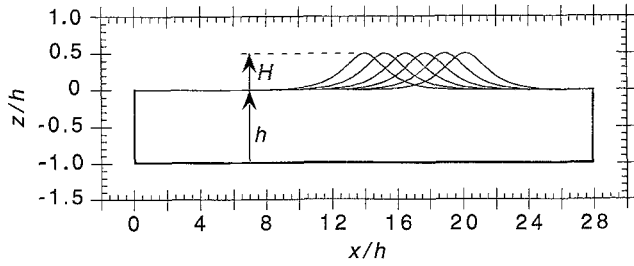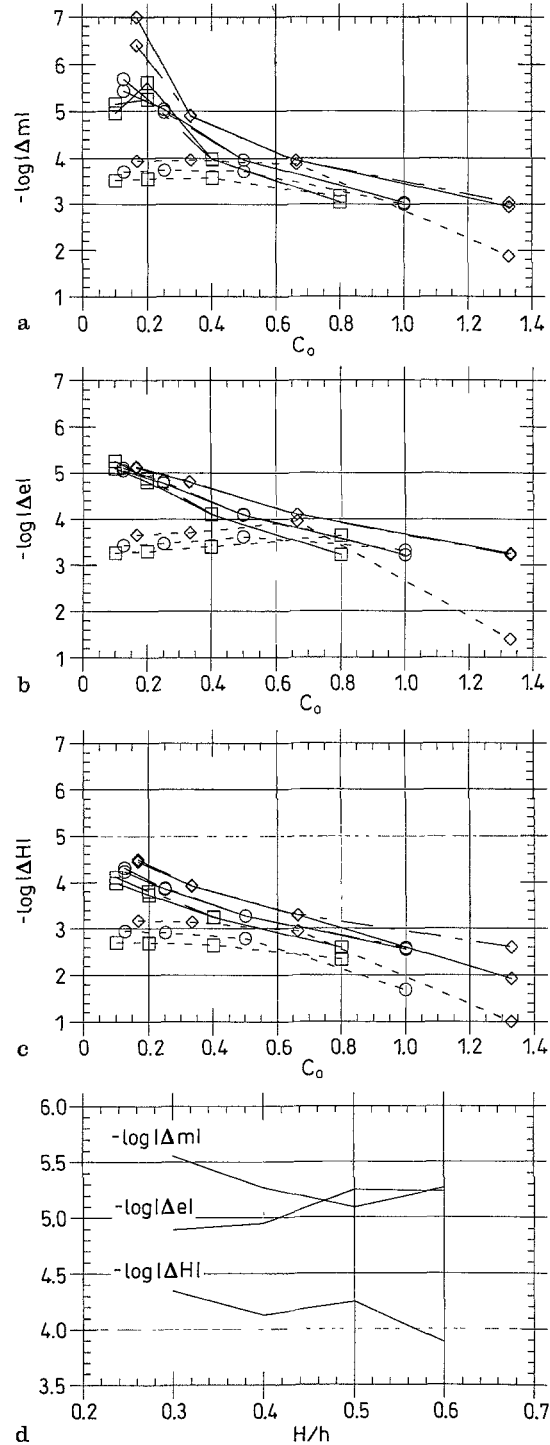
**Fig. 2.** Sketch of computational domain for the propagation of a fully nonlinear solitary waves of height $H/h = 0.3$–$0.6$, over 5 units of time (domain length is $L/h = 28$). Results are given in Fig. 3

$L/h = 28$ (with $h = 1$). Three different spatial discretizations are used in the computations, with initial distance between nodes on the free surface, $\Delta x_o' = \Delta x_o/h = 0.15, 0.20, 0.25$. In addition, $\Delta z' = 0.25$ on the lateral boundaries in each discretization and $\Delta x' = 0.25$ on the bottom, in the first set of results, and $0.40$ in the next two ones. The QS, MII, and MCI cubic interpolation methods are successively used on the free surface, while three-node quadratic isoparametric elements are used on other boundaries of the domain (Fig. 2). Ten Gauss points are used per element and adaptive integration is specified in corner elements.

Figures 3a–c show results for a solitary wave of height $H/h = 0.50$. The incident wave is introduced in the model with its crest at $x' = 14$ and is then propagated over 5 dimensionless time units (Fig. 2). Maximum absolute errors in wave volume $m$, total energy $e$, and wave height $H$ are calculated over this propagation time with respect to Tanaka's solution ($m = 1.7914787$, $e = 0.6157121$, and $H = 0.5000000$). Four different constant time steps are used in the computations[5], $\Delta t_o' = \Delta t_o\sqrt{g/h} = 0.025, 0.05, 0.10$, and $0.20$. Twelve cases with different spatio-temporal discretization are thus calculated using each interpolation method and errors are plotted in the figures, in negative logarithmic scales, as a function of $\Delta x_o'$ (symbols), the interpolation method (lines), and $\mathscr{C}_o = \Delta t_o'/\Delta x_o'$. Note that results with the QS method are identical to those in GS.

Results in Figs. 3a–c show that the MII and the MCI methods give similar errors in most cases (except for the largest Courant number) and that, for $\mathscr{C}_o \leq 0.5$, errors are reduced by up to 3 orders of magnitude as compared to the QS method. It should be stressed that these reductions in errors are obtained for essentially the same computation time. With the QS method, as expected from both the conclusions in GS and the discussion in Sect. 2.5, errors are minimum or level up for $\mathscr{C}_o \simeq 0.50$. With the MII and the MCI methods, only errors in volume in the coarser discretization reach a minimum (Fig. 3a) and, for the other tested cases, errors either do not reach a minimum or more or less level up for $\mathscr{C}_o \simeq 0.20$–$0.35$. This is because the more accurate solution of Laplace's equation with the MCI and MII methods leads to a slower rate of error accumulation, when many time steps are used. To avoid using too many small computational time steps, however, the upper bound of this interval, i.e., $\mathscr{C}_o \simeq 0.35$, will be used in later



**Figs. 3a–d.** Absolute numerical errors ($\Delta$'s) with respect to theoretical values by Tanaka: (abc) for $H/h = 0.5$; or (d) as a function of $H/h$. In (abc), errors in mass $m$, energy $e$, and height $H$, are given as a function of free surface interpolation method: (——) MCI; (—·—) MII; and (- - - -) QS, and the initial distance between nodes: $\Delta x_o' = $ ($\square$) $0.25$; ($\bigcirc$) $0.20$; and ($\diamond$) $0.15$. In (d), errors are given for $\Delta x_o' = 0.15$ (MCI interpolation) and $\mathscr{C}_o = 0.35$ (adaptive time step)

applications of the MII and MCI methods, in combination with the adaptive time step procedure (24). As pointed out in GS and seen in Fig. 3, accuracy can only be significantly improved around this selected value of $\mathscr{C}_o$ by using a smaller initial $\Delta x_o'$.

---

[5] Note that, as discussed in Sect. 2.5, the smaller the time step, the larger the number of time steps necessary to propagate the wave over the given time.

The influence of initial wave height – a measure of nonlinearity – on model accuracy is tested next and results are plotted in Figure 3d. Solitary waves of height $H/h = 0.3-0.6$, are propagated in the same domain as above (Fig. 2), using $\Delta x'_o = 0.15$, $\mathscr{C}_o = 0.35$, the adaptive time step procedure (24), and the MCI method for the interpolation on the free surface. Fig. 3d gives the same types of errors as in Figs. 3a–c. One can see that the model is almost uniformly accurate over the whole range of tested wave heights, up to fairly steep waves. One can also see, comparing results for $H/h = 0.5$, that errors are slightly smaller when using the adaptive time step scheme (Fig. 3d) than when using fixed time steps (Figs. 3a–c).

## 3.2
### Solitary wave shoaling and breaking over a gentle slope
Solitary waves are often used as a simple model for studying propagation, shoaling, and breaking of extreme waves in shallow water. Solitary waves closely model tsunamis and can also be used to represent surf-zone waves (see GSSV and Grilli, Svendsen and Subramanya (1994) for detail).

Computations of shoaling and runup of fully nonlinear solitary waves over a slope were reported by Svendsen and Grilli (1990) using the QS method and by OSG, using the MII method. These computations, however, were not performed for very gentle slopes which are more demanding cases, due to the quasi-singular situations in the BEM resulting from the very narrow geometry in the upper part of the slope. Grilli and Subramanya (1994) developed efficient methods for calculating quasi-singular integrals and, using the MCI method for the interpolation on the free surface, reported quite accurate results for the shoaling of solitary waves over a 1:35 slope. GSSV, following the same approach, calculated many detailed features of the flow under the crest of shoaling solitary waves, up to initiation of breaking by overturning of the crest. In all these cases, termination of calculations always occurred when, due to flow convergence in poorly resolved breaker jets, two nodes moved very close to each other thus creating an almost singular situation in the BEM, which led to very large errors and to the instability of computations. In fact, in all these applications, computations had to be stopped a short time after the wave crest started overturning, and no detailed analysis of the breaker jet could be made[6].

Errors in the BEM solution can be reduced in breaker jets without using a finer initial discretization over the whole free surface, which would be too computationally expensive, by: (i) using the more accurate MCI elements in the discretization instead of QS elements; (ii) improving the resolution by selectively adding nodes to the wave crest region (i.e., to only a small portion of the free surface); and (iii) limiting the occurrence of quasi-singular situations by preventing nodes from moving too close to each other (adaptive regridding). Benefits of using methods (i) to (iii) are illustrated in the following computations for the shoaling of solitary waves of initial height, $H'_o = H_o/h_o = 0.20$ and 0.40, over a 1:35 slope (i.e., in a set-up similar to the applications in GSSV). For each wave, two cases are calculated, either using the QS method or the MCI method for the interpolation on the free surface, and their accuracy is compared. Node regridding techniques introduced in Sect. 2.4 are then used to increase the resolution of the discretization in breaker jets, while preventing nodes from moving too close to each other. This allows calculations to be carried out for a longer time, within the same overall accuracy[7] (e.g. 1% maximum error on wave mass).

### 3.2.1
#### Comparison between the QS and MCI methods
The computational domain is sketched in Fig. 1. Since all tested waves break before reaching the top of the slope, the upper part of the slope, where the domain geometry becomes very narrow, was replaced by a small shelf of depth $h = 0.1\,h_o$ (i.e., for $x' > 41.5$). Unnecessary refinements of the discretization and of the integration methods in the upper part of the slope are thus avoided. It can be shown that reported results are not influenced by this slight change in geometry.
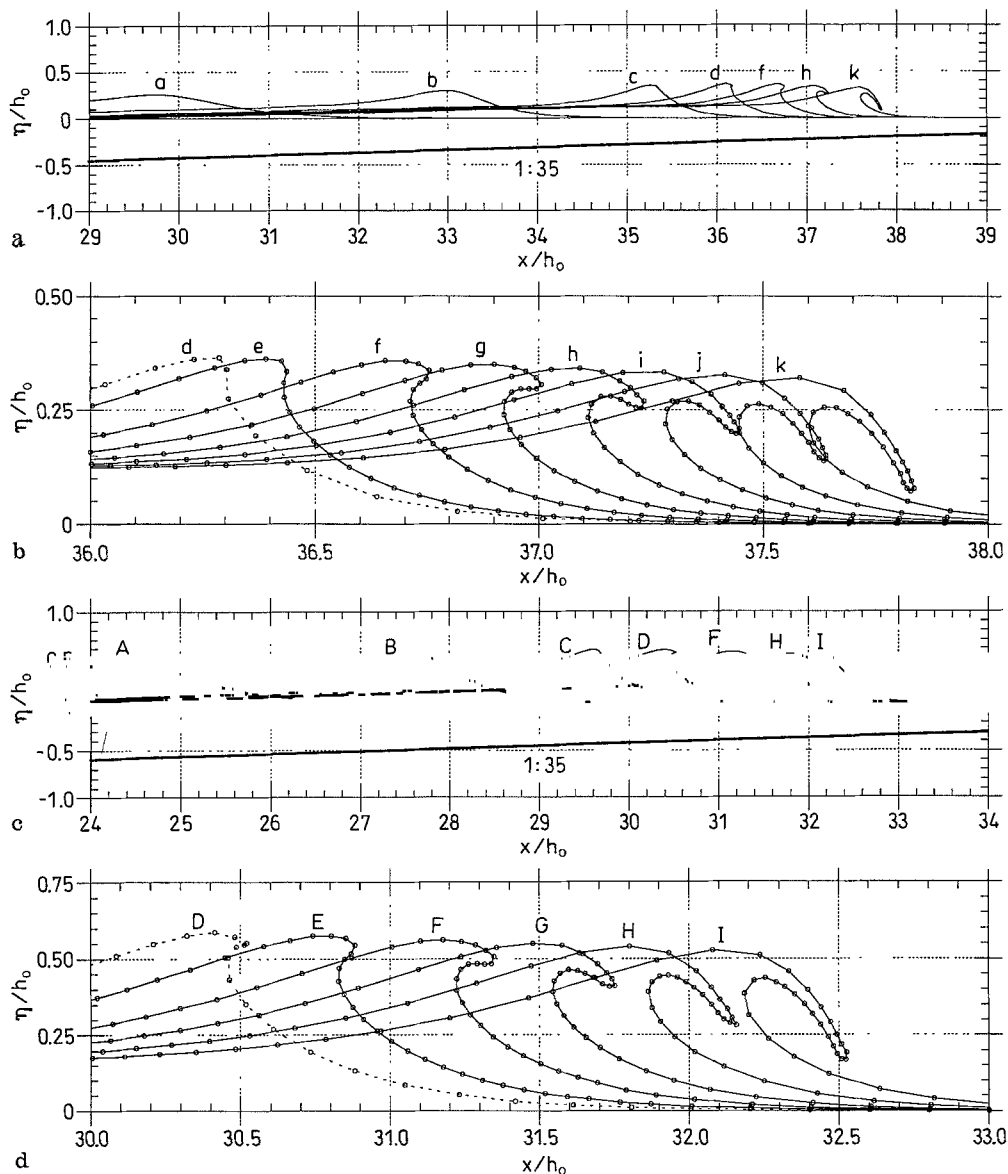
There are $N_\Gamma = 429$ nodes in the discretization, including $N_f = 226$ nodes on the free surface (with initial spacing $\Delta x'_o = 0.20$) representing $M_f = 225$ QS or MCI elements. There are $M = 100$ quadratic isoparametric elements on the bottom and lateral boundaries. The distance between nodes on the bottom is 0.5 in the constant depth region ($x' \leq 10$) and this distance is progressively reduced over the slope to 0.40, 0.25, 0.20, 0.15 and 0.10, in order to get increased resolution when depth decreases. On the shelf bottom, the distance between nodes is 0.15. Quasi-singular integration methods by Grilli and Subramanya (1994) are used in all corner elements and in free surface and bottom elements for which the local depth is equal to or smaller than the element length on the free surface, $\Delta x'_o$ (i.e., for $x' \geq 38$). The mesh Courant number is set to $\mathscr{C}_o = 0.35$ for both interpolation methods, which corresponds to $\Delta t'_o = 0.070$. With these data, the CPU time per time step is 12.9 sec (IBM 9000/3) for both the QS and the MCI methods[8].

Incident solitary waves are generated: (i) using the numerical piston wavemaker on the leftward lateral boundary of the domain, for $H'_o = 0.20$; or (ii) using the exact method by Tanaka (1986) in the constant depth region prior to the slope, for $H'_0 = 0.40$ (with the initial crest at $x' = 9$). Figures 4a (curves a–d) and 4c (curves A–D) show stages of wave shoaling and breaking calculated with the MCI method in the initial discretization, up to slightly prior the instant of instability of the computations. The breaking point, defined as the crest location for which the free surface slope becomes vertical in the wave front, is located at $x'_b = 36.3$ (reached at $t'_b = 44.53$) and $x'_b = 30.4$ (reached at $t'_b = 18.33$), for each wave respectively.

---

[6] In these computations, the poor resolution in the breaker jets resulted from the large horizontal extension of the discretized free surface in the computational domain (sometimes more than 100 water depths) which prevented a sufficient number of nodes from gathering in the wave crest region, before overturning was intiated, unless a prohibitive number of nodes was initially used over the whole free surface.

[7] Grilli, Svendsen and Subramanya (1994) and Wei, Kirby, Grilli and Subramanya (1995) also reported similar calculations of flow characteristics of shoaling solitary waves, up to and beyond the breaking point, over slopes 1:8 down to 1:100. These references can be consulted for more results and discussions on the physics of wave processes.

[8] It is again seen that the more accurate MCI method is not more computationally expensive than the QS method.

**Figs. 4a–d.** Blow-ups of Fig. 1 for the shoaling and breaking of solitary waves of initial height: (ab) $H_o' = 0.20$; and (cd) 0.40, over a 1:35 slope. Curves: a–d and A–D, are without regridding; e–k and E–I, are after regridding. ($\bigcirc$) denote discretization nodes, ($--\circ--$) represent last computed profile without regridding, and ($-\circ-$) represent regridded profiles. Time of plotted wave profiles is $t' = a$: 37.17, $b$: 40.73, $c$: 43.48, $d$: 44.53, $e$: 44.62, $f$: 44.94, $g$: 45.20, $h$: 45.40, $i$: 45.60, $j$: 45.80, $k$: 46.00, $A$: 13.15, $B$: 16.00, $C$: 17.67, $D$: 18.33, $E$: 18.66, $F$: 19.00, $G$: 19.30, $H$: 19.60, and $I$: 19.90. Corresponding numerical errors are plotted in Fig. 5
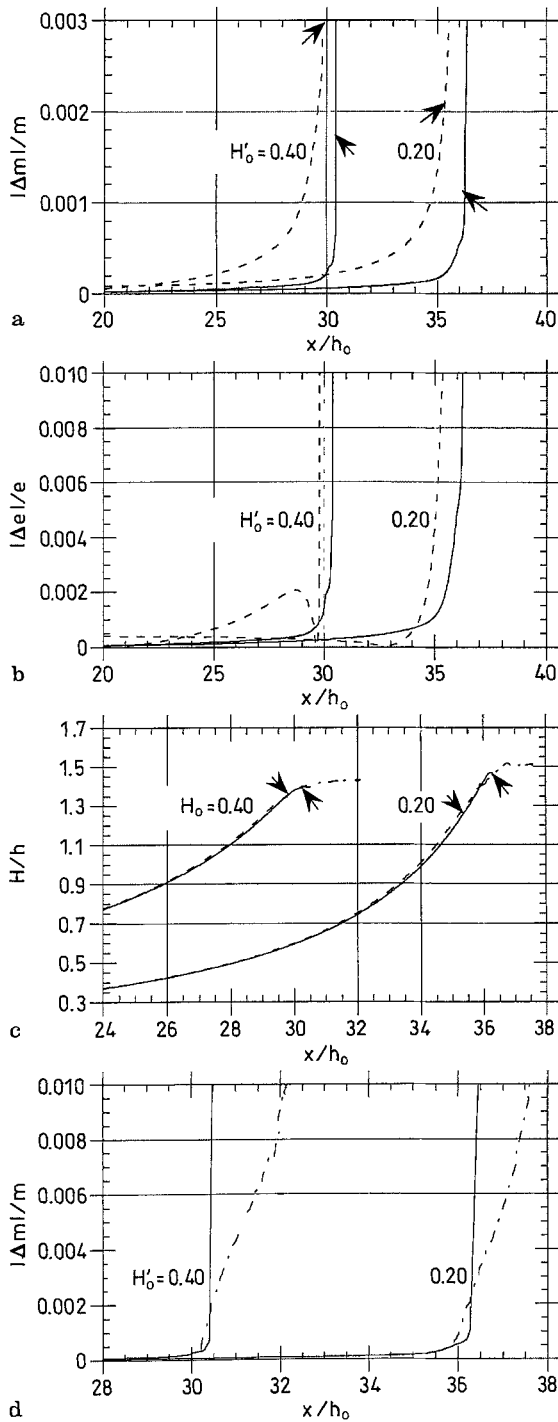
Corresponding breaking wave heights and breaking indices are: (i) $H_b' = 0.364$, $H_b/h_b = 1.46$; and (ii) $H_b' = 0.587$, $H_b/h_b = 1.41$, respectively. During propagation, time step reduces to $\Delta t' = 0.019$ and 0.0003, at the time of breaking, for each wave respectively. The total number of time steps up to the breaking point is 950 and 750 and the average time step is 0.047 and 0.024 for each case, respectively.

Figures 5a and 5b give numerical errors in wave mass and total energy for the QS and the MCI methods. For most of the wave propagation, these errors are much smaller using the MCI method than using the QS method. Hence, for a pre-specified maximum numerical error (e.g., 1%), wave propagation can be calculated for a longer time with the MCI method before computations are deemed inaccurate. Figure 5b shows that, for both interpolation methods, the energy error first reaches the 1% threshold and, as expected, this occurs quite earlier with the less accurate QS method. Arrows in Fig. 5a show locations for points of maximum energy error. Figure 5c gives relative wave heights $H/h$ as a function of $x'$,

for both interpolation methods. Arrows again indicate locations at which energy errors reach 1% in the computations. As expected, using the MCI method, shoaling is calculated for a longer time within the required accuracy[9].

In the last stages of shoaling, discretization nodes converge towards wave crest regions while the distance between nodes increases in the front and in the back of the waves. This is quite apparent in Figs. 4b and 4d (dashed curves d and D). Despite this node concentration, however, when breaker jets start forming at the tip of the crests, the discretization is not sufficiently resolved to allow formation of large scale plunging jets. Hence, numerical errors quickly increase leading to instability of computations (as seen in Figs. 5a–b). This can be improved using the node regridding techniques.

[9] Note that (more accurate) shoaling curves calculated with the MCI method are slightly lower than with the QS method. This agrees to within 2% with measurements by GSSV, up to the breaking point.

Figs. 5a–d. Shoaling of solitary waves of initial height $H'_o$ over a 1:35 slope: (a), (d) relative errors on wave volume $m$; (b) relative errors on total energy $e$; and (c) shoaling curves $H/h$. Free surface interpolation method: (—) MCI; (— — — —) QS; (—·—) MCI with regridding. Arrows in Fig. 5ac indicate locations at which errors on total energy reach 1.0% in Fig. 5b

### 3.2.2
### Regridding of the breaker jet

Node regridding is used to improve resolution of computations (and thus numerical accuracy) in the last stages of wave shoaling and breaking. For both waves, 40 nodes are added to a free surface segment containing the wave crest, at a time

slightly before reaching the breaking point and the steep increase in computational errors observed in Figs. 5a–b (i.e., at $t' = 44.12$ and 18.15 respectively). These nodes are regridded to constant arc length intervals together with "old" nodes in the sections. Regridded sections thus span from $x' = 33.26$ to 37.80 and $x' = 25.84$ to 32.00, and the number of "old" nodes in these sections is 31 and 37, for each wave respectively[10]. After regridding, the total number of nodes in the discretization is 469 and the CPU time per time step increases to 14.8 sec. To reduce quasi-singularities due to node proximity in regridded breaker jets, the adaptive regridding procedure is used for the computations in the regridded discretizations to check distances between nodes and regrid nodes two-by-two if needed.

Due to regridding, the minimum distance between nodes increases in the discretizations. Hence, assuming that, for stability reasons, computations are resumed in the regridded domain with a time step equal to its value prior to regridding (i.e., $\Delta t' = 0.0103$ and 0.0014 for each wave respectively), Eq. (24) implies that the mesh Courant number must decrease. Although computations using a smaller Courant number are still accurate (see Sect. 3.1), this may lead to an unnecessary large number of time steps, and, eventually, to an accumulation of numerical errors. To avoid this problem, after regridding, the Courant number is increased back to 0.35 over 10 computational steps, following a smooth "tanh" law variation, and the time step is correspondingly increased. After regridding, 280 and 200 additional computational steps are thus calculated for each wave, respectively, and corresponding time step values reduce to $\Delta t' = 0.0043$ and 0.0061. Wave profiles computed in the regridded discretizations are shown in Fig. 4, curves e–k and E–I, and corresponding errors in wave mass are given in Fig. 5d and compared to errors obtained for the same waves without regridding (note that errors in wave energy are about 5 times as large as these). Last plotted profiles in Fig. 4 (curves k and I) correspond to a 1% error in wave mass[11].

Figure 5d shows that, within a 1% accuracy on wave mass, computations can be pursued for a longer time and over a larger distance of propagation in the regridded discretizations, up to the theoretical limit of FNPF theory (i.e., the instant the tip of the breaker jet is about to impact the free surface:curves k and I), for only a very marginal increase in computational effort. Results in Figs. 4b and 4d, in the regridded discretizations, show the development of well resolved breaker jets. Figure 5c shows that, in this post-breaking region, breaking indices reach an almost constant value. Both waves, finally, exhibit well known features of plunging breakers over

---

[10] Free surface shapes and node locations before and after regridding are very similar to those shown in curves d, e and D, E of Figs. 4a–b, for each wave respectively.

[11] Note that computations by Subramanya and Grilli (1994), in which regridding was performed at the breaking point using a larger number of "new" nodes (49) and over a narrower region of the free surface (mostly in front of the wave crest), showed that both numerical errors could be cut to about one-fourth the present case and free surface profiles obtained were closely identical to those in Fig. 4. This illustrates the convergence of numerical procedures used for computing the solution in breaker jets.

gentle slopes (Peregrine (1983)), with a large scale plunging of the wave crest and quasi-elliptical areas enclosed below the breaking jets ("pipelines"). Grilli, Svendsen and Subramanya (1994) discussed the physics of these and other similar results and showed that they agree quite well with experimental data from various sources.

## 3.3
## Wave breaking induced by a moving boundary
Problems with strong interactions between a moving boundary and a free surface are quite frequent and important ones in ocean engineering. To name but a few of these: the generation of a (possibly breaking) bow wave by a forward moving vessel, the slamming of a ship hull on the ocean surface, or the generation of waves by a wavemaker in a laboratory wave tank.

When a lateral vertical boundary of the computational domain, say $\Gamma_{r1}$ in Fig. 1, is moved from a state of rest with sufficient acceleration, the free surface close to the intersection with the boundary quickly rises upward and also acquires a large horizontal acceleration. Possible mathematical or numerical singularities of the solution in the corner representing the intersection between the free surface and the lateral boundary were discussed in the introduction and in Sect. 2.6. It was seen that, provided initial boundary conditions are well-posed (thus eliminating initial (mathematical) singularities) and BEM numerical integrations are accurate, compatibility conditions could be used to ensure instantaneous well-posedness of boundary conditions at corners and avoid the occurrence of (numerical) singularities through time stepping. Doing so, very accurate results could be obtained at corners (GS, OSG).

The initial mathematical singularity of the solution and its treatment in the model are discussed in the next Section. Various numerical tests are then carried out to assess accuracy of results obtained using new corner compatibility conditions (27) versus the old condition (25), new surface interpolation methods, MII and MCI, versus QS, and new regridding techniques. It should be pointed out that, in the following, the purpose of regridding is to improve result accuracy in two situations: (i) in a given discretization, by adding nodes to insufficiently resolved free surface regions (e.g., close to the wavemaker); and (ii) in a coarse discretization, by selectively adding nodes to specific boundary segments (e.g., wavemaker, wave crest), thereby obtaining results comparable to those in a finer discretization, with a reduced computational effort[12].

## 3.3.1
## Wavemaker motion and initial boundary conditions
When waves are generated from a state of rest using a wavemaker, there is an initial jump to finite values of the wavemaker velocity and acceleration, at the first time step of computations (on boundary $\Gamma_{r1}$, Fig. 1), whereas initial potential $\phi(x,0)$ and elevation $\eta(x,0)$ are normally set to zero on the free surface (boundary $\Gamma_f$). This creates conflicting boundary conditions on both sides of a corner which, in fact, are similar to the step velocity case studied by Roberts (1987) based on a small time weakly nonlinear analysis. Roberts'

results showed that conflicting initial boundary conditions create a singularity associated with fast small scale oscillations of the free surface close to the wavemaker[13]. The same study also predicted non singular behavior for an initial wavemaker velocity starting from zero and exponentially increasing with time. The latter result should be expected since, in this case, both the initial velocity and the acceleration are zero and the initial boundary conditions are well posed. The disadvantage of such an approach, however, as pointed out in OSG, is that it would take an infinite time for the wavemaker to reach a finite velocity.

With these observations in mind, GS studied the accuracy of the solution close to the wavemaker, when generating first-order (Boussinesq) solitary waves with a piston wavemaker moving as,

$$x_p(t) = \frac{H_o}{\kappa} \left[ \tanh \frac{\kappa}{h_o} (ct - x_p(t) - \lambda) + \tanh \frac{\kappa\lambda}{h_o} \right] \qquad (28)$$

in which $H_o$ is the wave height in constant depth $h_o$, $\kappa = \frac{1}{2}\sqrt{3H_o'}$, and the celerity $c = \sqrt{g(h_o + H_o)}$. Piston motion (28) corresponds to a wave profile truncated at distance $\lambda$ on both sides of the wave crest, where free surface amplitude has reduced to $\varepsilon_z H_o$. Developing (28), the initial wavemaker acceleration reads,

$$\dot{u}_p(0) = \sqrt{3} g \varepsilon_z (H_o')^{3/2} (1 + H_o') \frac{(1 - \varepsilon_z)^{1/2}}{(1 + \varepsilon_z H_o')^2} \qquad (29)$$

which, for small $\varepsilon_z$ and fixed $H_o'$, is roughly proportional to $\varepsilon_z$ and can thus be made arbitrarily small (initial velocity is also roughly proportional to $\varepsilon_z$)[14]. Thus, for small $\varepsilon_z$ (i.e., for large $\lambda$), both the initial velocity and acceleration are small but finite and the piston motion subsequently follows a smooth "tanh" law (with initial exponential increase).

When generating solitary waves using a small $\varepsilon_z$ value (typically 0.002) corresponding to an initial acceleration much smaller than gravity, GS obtained fairly smooth free surface profiles close to the wavemaker and concluded that, for all practical purposes, limiting the initial acceleration to a small fraction of $g$ was sufficient to eliminate initial singularity problems[15]. In a more detailed analysis of these results, however, OSG showed that small oscillations do occur on the free surface close to the wavemaker, first in the higher-order derivatives of the potential ($\partial^2\phi/\partial t\partial n, \partial^2\phi/\partial s^2$), and propagate downstream with the generated wave. This is a clear indication of initial singularity problems. In the model, however, it takes a fairly large distance of propagation for these oscillations to grow and to significantly affect the wave profile. In the light of theroetical conclusions above, OSG re-calculated the

---

[13] Note that, due to these fast oscillations, nonlinear and surface tension effects should play a role and should also be included in the analysis. This was somewhat improved in the solution of the same problem by Joo, Schultz and Messiter (1990) which included surface tension effects.

[14] For small $\varepsilon_z$, $\dot{u}_p(0) \simeq \sqrt{3}\varepsilon_z (H_o')^{3/2}(1 + H_o')g$ (with, e.g., $\lambda = 3.8\,h_o/\kappa$ for $\varepsilon_z = 0.002$).

[15] This also qualitatively agreed with Roberts' (1987) conclusions when the exponent in his power law was greater than 2.

---

[12] This situation is similar to the shoaling computations in Sect. 3.2

generation of a fairly large wave ($H'_o = 0.4$), using a much smaller $\varepsilon_z = 3.5 \cdot 10^{-5}$ ($\lambda = 5.8 h_o/\kappa$) corresponding to a very small initial acceleration, $\ddot{u}_p(0) = 2.2 \cdot 10^{-5} g$. Doing so, initial inconsistencies in boundary conditions were very much reduced and results indeed showed that oscillations in higher-order derivatives were eliminated. Initiation of the wavemaker motion and wave generation, however, took a much larger time than when using a larger $\varepsilon_z$.

To be able to use larger $\varepsilon_z$ values and thus reduce the wave generation time, OSG proposed to initiate their calculations with consistent boundary conditions on the free surface, by specifying both a small initial elevation and potential on the free surface corresponding to the initial velocity $u_p(0)$ and acceleration $\ddot{u}_p(0)$ of the wavemaker. To do so, they assumed exponential forms for $\eta(x,0)$ and $\phi(x,0)$ and, for small initial amplitudes, they solved the corresponding linearized problem and obtained,

$$\eta(x,0) = \frac{\ddot{u}_p(0)}{2\kappa g} e^{-2\kappa x}, \quad \phi(x,0) = -\frac{u_p(0)}{2\kappa} e^{-2\kappa x} \quad (30)$$

Using (30) as initial conditions on the free surface and re-calculating cases above, they showed that oscillations could be eliminated for $H'_o = 0.4$, even with $\varepsilon_z = 0.002$, which confirmed that initial (mathematical) singularities were effectively removed. This method is used in the present computations.

When eliminating the initial (mathematical) singularity as described above, the impulsive flow induced by a strongly moving boundary constitutes a very demanding numerical test case for the accuracy of compatibility conditions in the free surface corner and also one that requires the discretization in this area to be sufficiently fine, due to large flow variations close to the corner, and the BEM integrals, particularly the quasi-singular ones, to be calculated with great care and accuracy. In the study by GS, a very large wave height, $H'_o = 2$, was selected in (28) (with $\varepsilon_z = 0.002$) in order to generate a wave that rapidly overturns and breaks quite close to wavemaker[16]. This case is re-computed here in order to test the accuracy of both the new interpolation methods and new corner compatibility conditions, versus older methods used in GS. Equations (30) are used as discussed above to eliminate initial singularities in the computations[17]. After carrying out these calculations in the same two discretizations as in GS, various node regridding strategies are tested in order to improve both the accuracy and the stability of results in the coarser discretization.

### 3.3.2
### Numerical data and preliminary computations
The computational domain is rectangular (as in Fig. 2) with a depth $h_o = 1$. Two spatial discretizations are used in the

computations: (i) a coarse one with node spacing $\Delta x'_o = 0.25$ on the free surface and on the bottom and a domain length $10 h_o$; and (ii) a fine one with $\Delta x'_o = 0.10$ on the free surface and on the bottom, and a domain length $8 h_o$[18]. In the first case, $\Delta z'_o = 0.125$ on lateral boundaries and, in the second case, $\Delta z'_o = 0.10$. The total number of nodes is $N_\Gamma = 100$ and $184$, for each case respectively. As in GS, two-node linear elements are used on lateral boundaries and on the bottom, and adaptive integration is specified in all corner elements. With these data, the computation time is 0.80 and 1.90 sec per time step (IBM 9000/3), for each discretization respectively. The free surface interpolation and the size of the time step are discussed in the following.

A large wave is generated in both discretizations by moving the lateral boundary according to (28), with $H'_o = 2$. Figure 6 shows free surface profiles computed with the MCI method (with $\mathscr{C}_o = 0.40$), using the new compatibility condition (27) in free surface corners. As expected, due to the strong movement of the lateral boundary, the generated wave overturns with a large scale plunging jet[19]. Figures 6a-b show results in the finer discretization and Fig. 6c. shows results in the coarser discretization. Figure 6d is a comparison between results in both discretizations. In the coarser discretization, likely due to insufficient resolution in the breaker jet, computations become inaccurate and have to be stopped at an earlier stage (curve i) than in the finer discretization (curve j) where computations can accurately be pursued up to impact of the breaker jet on the free surface (the theoretical limitation of FNPF models). The latter is a marked improvement versus computations in GS, using the QS method in the finer discretization, which had to be stopped at the stage of curve f. Accuracy of computations in the coarser discretization will be improved by regridding (Section v below). Figure 6d shows that, for curves a—i, results obtained with both discretizations are in quite good agreement, except close to the wavemaker and in the jet regions (assuming reflection in the wave front is ignored).

### 3.3.3
### Comparison between the old and the new corner compatibility conditions
To test the old corner compatibility condition (25) used in GS (subscript $o$) versus new condition (27) (subscript $n$), computations are carried out in both discretizations using the QS interpolation method on the free surface, with $\mathscr{C}_o = 0.32$ (subscript 1) and 0.40 (subscript 3). Relative errors in wave mass[20] are given in Fig. 7a as curves ($QS_{1o}, QS_{1n}$) and ($QS_{3o}, QS_{3n}$). Comparing these curves two-by-two for both discretizations, it is clear that using new corner compatibility conditions leads to more accurate results and to longer
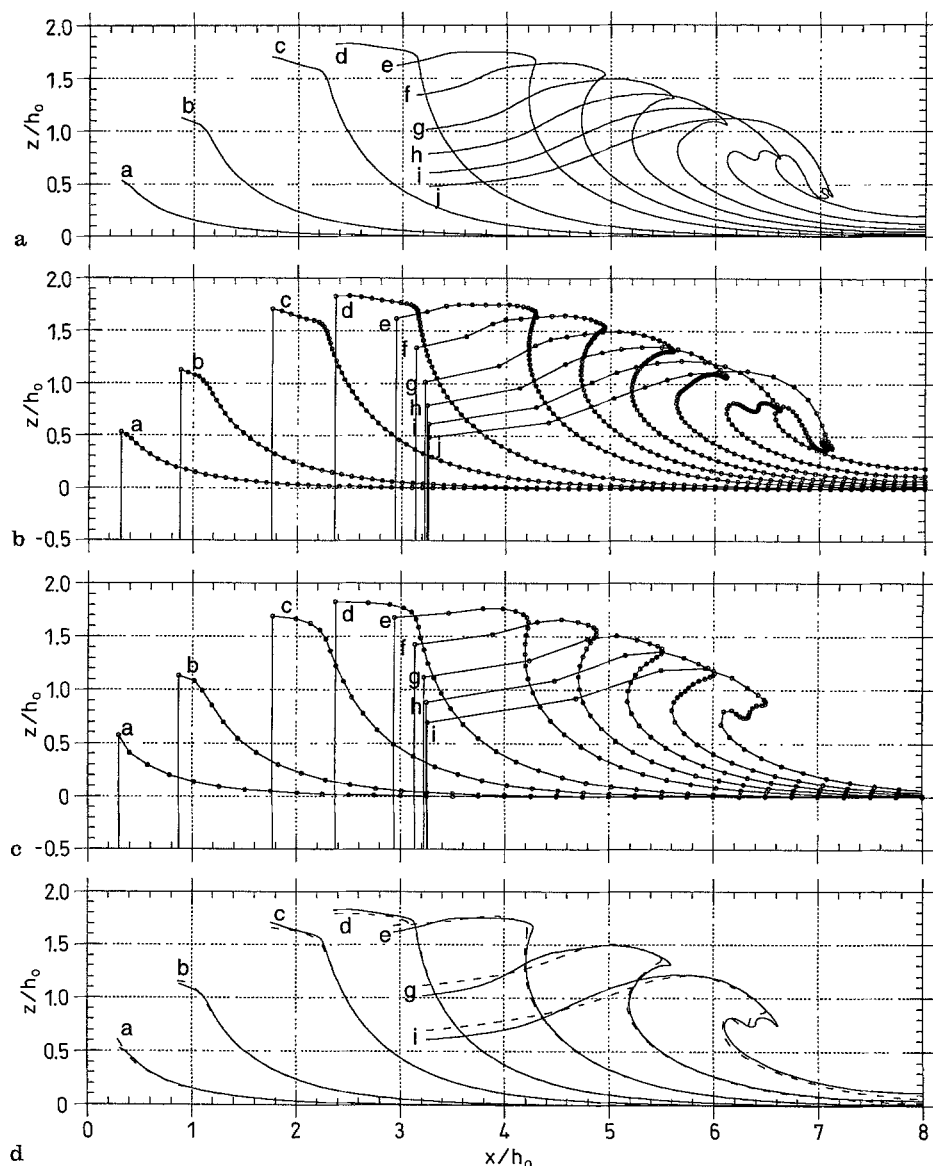
---

[16] In this case, although maximum wavemaker acceleration reached one $g$, the initial acceleration given by (29) was still small, only about $0.03 g$.

[17] Note, however, in the present case, due to the short propagation distance (and propagation time) of generated waves, initial small oscillations in $\phi_{tn}, \phi_{sg}$, obtained for $\varepsilon_z = 0.002$ when initialization (30) is not used, would not significantly affect global accuracy of computations.

[18] The shorter computational domain was selected in the finer discretization to reduce computational time. This will not influence results at all in the region up to and including the breaker jet, in the last computed profile. Reflection will only slightly increase in the wave front, for $x' > 7$ or so, and will lead to small discrepancies in free surface elevation between results computed in both discretizations.

[19] Note the bimodal tip of the breaker jet, resulting from the somewhat unusual way of generating breaking with a piston wavemaker.

[20] With $m = 3.26$, the maximum wave mass above the undisturbed free surface $z = 0$.

**Figs. 6a–d.** Wave breaking induced by a piston wavemaker (solitary wave motion with $H_o' = 2.0$) with: $\Delta x_o'$ and $\mathscr{C}_o =$ (a)(b) 0.10, 0.40; (c) 0.25, 0.40. (d) shows superimposed results of: (—) (a), (b) and (----) (c). (○) denote discretization nodes and vertical lines mark successive locations of the piston wavemaker. Time of plotted wave profiles is $t' = a$: 1.442, $b$: 2.064, $c$: 2.843, $d$: 3.381, $e$: 4.011, $f$: 4.353, $g$: 4.681, $h$: 4.936, $i$: 5.191, $j$: 5.438

propagation times before instability occurs than using the old conditions.

### 3.3.4
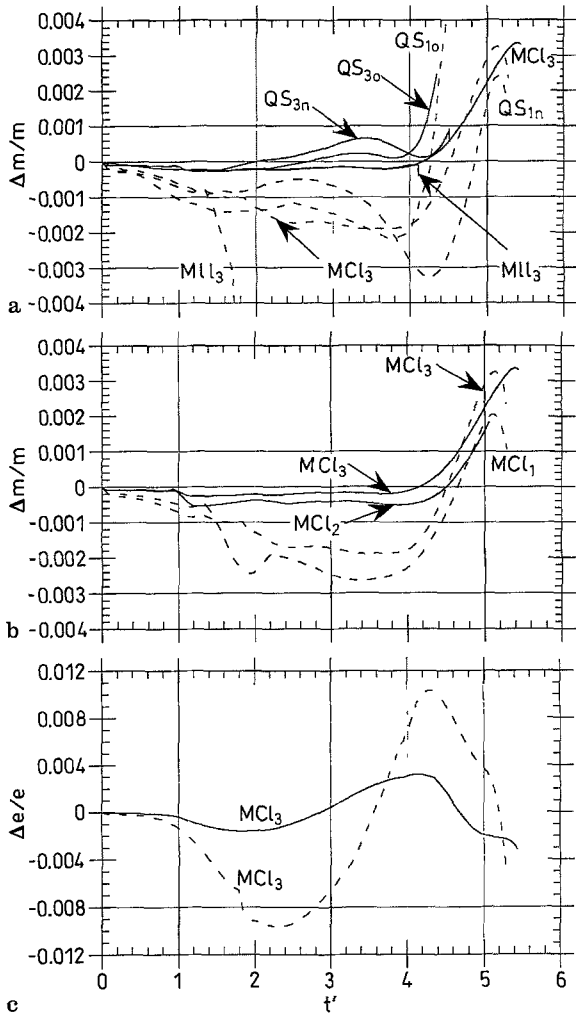### Comparison between the QS and the MII and MCI interpolation methods

To assess the accuracy of new interpolation methods on the free surface, computations are carried out using the QS, MII, and MCI interpolation methods, with the new corner compatibility condition (27) and a mesh Courant number equal to 0.40 (subscript 3).

Relative errors in wave mass are given in Fig. 7a for these computations. They show that results obtained with the MII method, although initially almost identical to those obtained with the MCI method, quickly become unstable in both discretizations whereas results with the MCI method can accurately be calculated for a longer time. In the finer discretization, the instability with the MII method occurs shortly after the wave reaches the breaking point (curve e in

Fig. 6), hence, even before the breaker jet starts forming, indicating that the instability is not due to problems in the breaker jet. More likely, as nodes move away from the wavemaker (due to node drift), results in the first interval of the first MII element on the free surface are getting increasingly poor. With time, this leads to an accumulation of errors in the corner and, eventually, to the instability of computations. The spline-based MCI method, on the other hand, does not extrapolate the geometry close to the corner and, hence, is not so sensitive to a loss of resolution of the discretization. As expected from shoaling computations in Sect. 3.2, MCI results are also more accurate than those obtained with the QS method. These conclusions justify the implementation of the MCI method for problems with moving solid boundaries.

The influence of the mesh Courant number on the accuracy of results with the MCI method is illustrated in Fig. 7b. In both discretizaions, the smallest errors and the longest propagation times are obtained using the largest Courant

Figs. 7a-c. Relative errors in mass $m$ and total energy $e$ for the calculations in Fig. 6 with $\Delta x'_o =$ (—) 0.10; (----) 0.25, for three interpolation methods: QS, MII, and MCI. Subscripts refer to: (i) $\mathscr{C}_o =$ (1) 0.32; (2) 0.35; (3) 0.40; (ii) Node compatibility = ($o$) old method; ($n$) new method (also used if nothing else is mentioned)

Finally, whereas relative errors on wave volume at the end of calculations are on the same order in both discretizations ($\sim 0.3\%$, in Figs. 7a-b), energy errors are more than three times larger in the coarser discretization than in the finer discretization (Fig. 7c). This is because the poorer resolution on the free surface in the coarser discretization leads to less accurate results for the kinematics and, hence, for the wave energy.
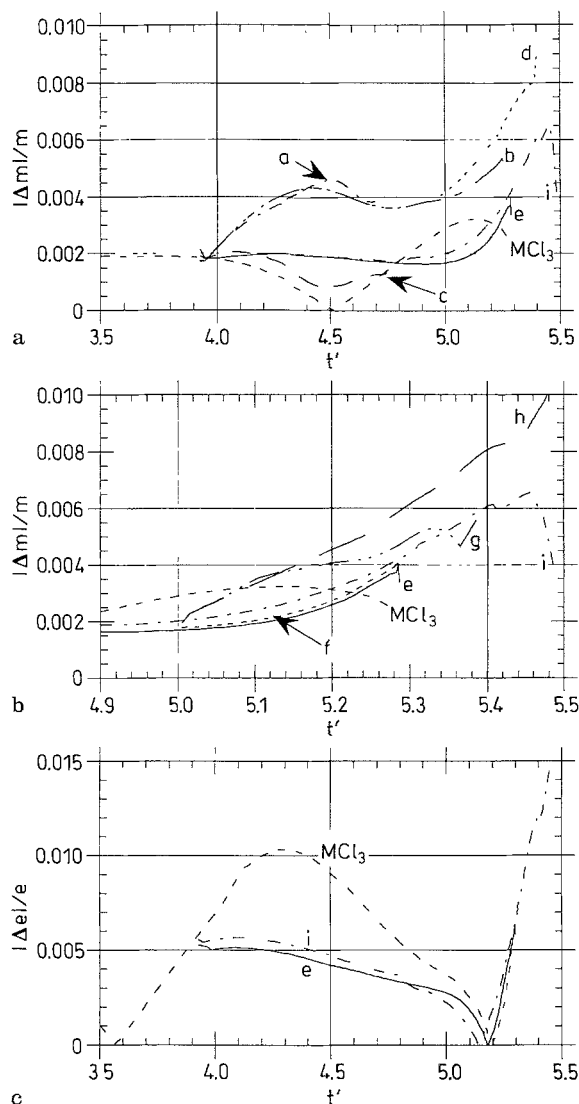
### 3.3.5
### Node regridding close to the wavemaker and in the breaker jet

In previous computations, numerical errors mainly resulted from a lack of resolution of the discretization close to the wavemaker, due to node drift (Fig. 6b-c, curves a-j), and from quasi-singular situations created in breaker jets, due to node proximity. Regridding will now be used to selectively add nodes close to the wavemaker, on the free surface, and adaptive regridding will be used to prevent nodes from moving too close to each other in breaker jets. Various regridding strategies addressing these problems (Table 1, a-i) were tested in the coarser discretization ($\Delta x'_o = 0.25$), using the $MCI_3$ method, and corresponding numerical errors and wave profiles are given in Figs. 8 and 9, respectively. Time $t'_1 = 3.93$ for the first regridding corresponds to the breaking point (vertical wave front, i.e., approximately curve e in Fig. 6). Errors in Fig. 8 give a measure of the effectiveness of each regridding method in allowing computations to be carried out in the coarser discretization, with sufficient accuracy, for a time longer than without regridding (curve $MCI_3$).

In Fig. 8a, strategies a or b (i.e., a simple regridding of the whole free surface without/with adjustment of $\mathscr{C}_o$) lead to increased errors without allowing computations to be carried out for a longer time. This is likely because breaker jets are regridded to too large a node interval. Strategy c (i.e., regridding of just the first 7 nodes) does not initially increase errors–since the breaker jet is not regridded–but leads to instability of computations at an early time. Strategy d (i.e., the addition of 10 nodes close to the wavemaker at later time $t'_2$ after regridding of the whole free surface at $t'_1$) allows computations to be carried out for a slightly longer time than without regridding, but final errors are more than three times as large. Strategy e (i.e., the addition of 10 nodes close to the wavemaker at time $t'_1$) leads to more accurate results for most of the propagation (the error curve in Fig. 8a is almost

number, $\mathscr{C}_o = 0.40$. In fact, as discussed in Sect. 3.1, using too small a Courant number leads to an unnecessary large numbers of time steps and to an accumulation of numerical errors.

| Strategy | Description of regridding strategy |
|---|---|
| a | At $t = t_1$, regridding of the free surface to constant step. |
| b | At $t = t_1$, regridding of the free surface to constant step, $\mathscr{C}_o = 0.40$. |
| c | At $t = t_1$, regridding of the first 7 nodes to constant step. |
| d | Same as $b$ and, at $t = t_2$, add and regrid 10 nodes to the first 6 node segment. |
| e | At $t = t_1$, add and regrid 10 nodes to the first 6 node sgement. |
| f | Same as $e$ and, at $t = t_2$, add and regrid 10 nodes to the first 6 node segment. |
| g | Same as $e$ and, at $t = t_2$, regrid first 30 node segment to constant step, $\mathscr{C}_o = 0.40$. |
| h | Same as $e$ and, at $t = t_2$, regrid first 30 node segment to constant step. |
| i | Same as $e$ and, for $t > t_1$, adaptive regridding on the free surface. |

Table 1. Regridding strategies for the computations in Figs. 8 and 9, with $MCI_3$ and $\Delta x'_o < 0.25$ (coarse grid). Regridding times: $t'_1 = 3.93$, and $t'_2 = 5.00$

**Figs. 8a–c.** Relative errors in the coarser discretization, for the same calculations as in Figs. 6-7, using regridding strategies (a-i) in Table 1 with MCI$_3$ and $\Delta x'_o = 0.25$. Curves MCI$_3$ correspond to results obtained without regridding

flat), but computations cannot be carried out for a longer time than without regridding. Figure 9a shows that the last computed wave profile in this case (curve B) is in good agreement with results in the finer discretization. Some discrepancies are still observed close to the wavemaker but are smaller than without regridding (see Fig. 6d). Strategy f, (a variation on strategy e that adds 10 more nodes close to the wavemaker at a later time $t'_2$) does not further improve the accuracy.

In Fig. 8b, strategies g or h (performing additional regridding of the first 30 nodes including the breaker jet at time $t'_2$ with/without adjustment of $\mathscr{C}_o$) allow computations to be carried out for a time almost as long as in the finer discretization ($t' = 5.35$) but with slightly larger errors. Figures 9b–c show that the last computed wave profiles in these cases (curves B) are in good agreement with results in the finer discretization. In strategies g and h, regridding of the breaker jet at time

$t'_2$ actually reduces the tendency of nodes to move too close to each other and thus also reduces quasi-singular situations. A better way of achieving this is to use the adaptive regridding method that checks node distance at all time steps and regrids nodes two-by-two if needed. This is finally done in strategy i, which combines strategy e to improve resolution close to the wavemaker and the adaptive regridding to improve accuracy in the breaker jet. Error curves in Fig. 8 for strategy i clearly give the best accuracy and the longest propagation time of all regridding method – in fact as long as in the fine discretization. Final error on wave mass is similar to the error in the fine discretization but the error on total energy is larger. Figure 9d shows that wave profiles computed with strategy i agree quite well with those obtained in the finer discretization, up to impact of the jet (curve j). Only the smaller scale features, like the bimodal breaker jet, are not represented due to insufficient resolution. Comparing curves e in Fig. 6c and 9d, one also sees how regridding has added nodes in the back of the wave and, comparing curves f–i in both figures, how nodes have now moved much less apart, close to the wavemaker.
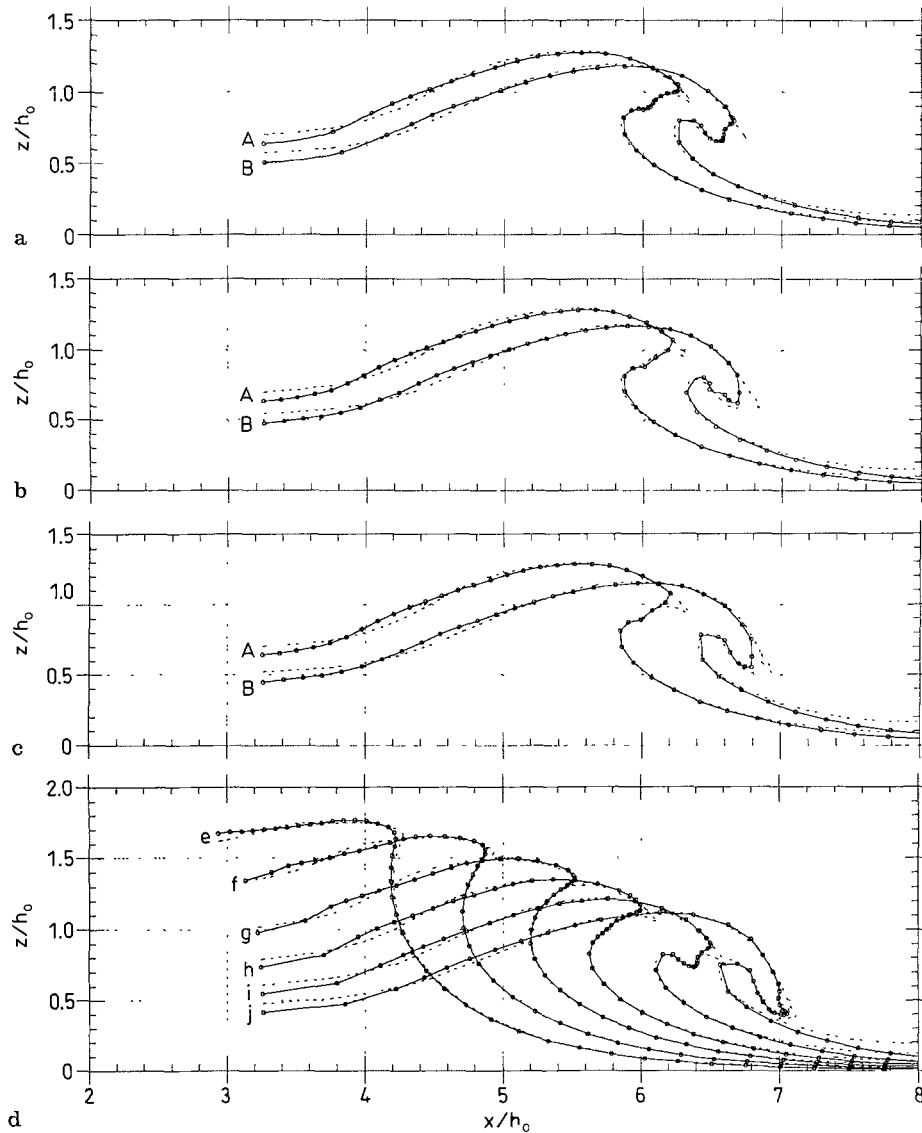
Finally, it should be stressed that results obtained with strategy i are calculated in a discretization that has only 10 more nodes than the original coarse discretization (total 110). This leads to a slight increase in computation time to about 0.95 sec per time step, i.e., only half the time needed in the finer discretization. Hence, using the regridding techniques, accurate results can be obtained in a coarser discretization with a much reduced computational effort.

## 4
## Conclusions

New interpolation methods and corner compatibility conditions were implemented in an existing fully nonlinear wave propagation model based on a BEM. Results showed improvements in both accuracy and stability of computations for wave breaking induced by fixed or moving boundaries, as compared to earlier methods. These improvements are achieved within essentially the same CPU time (i.e., computational effort) as with the earlier model. New numerical methods are thus also found to be more efficient.

Node regridding techniques were implemented to further improve both the accuracy and the duration of computations before numerical instabilities occur. These techniques selectively add and redistribute nodes over specified sections of the free surface and/or adaptively regrid nodes two-by-two on the free surface when they move too close to each other. The combination of regridding techniques with new interpolation and corner compatibility methods allows computations of wave breaking (induced by a bottom slope or by a moving boundary) to be accurately pursued beyond the breaking point (vertical front slope of the wave), up to impact of the breaker jet on the free surface (theoretical limitation of FNPF theory).

With the earlier model, calculations in large computational domains, in particular, had to be stopped at or shortly after the breaking point was reached thus preventing a close analysis of post-breaking wave characteristics. This is now possible using the new methods and present results, for instance, show the detailed development of the plunging

Figs. 9a–d. Free surface profiles obtained for the same calculations as in Fig. 8 using regridding method: (a) $e$; (b) $g$; (c) $h$; (d) $i$, compared to computations in the fine discretization (- - - -) with $MCI_3$ (no regridding, also shown in Fig. 6a). ($\bigcirc$) denote discretization nodes and results. Time of plotted wave profiles is $t' =$ (a) $A$: 5.05, $B$: 5.25; (b), $A: = 5.05$, $B$: 5.30; (c) $A$: 5.05, $B$: 5.35; (d), e–j as in Fig. 6

breaking of solitary waves over a gentle slope. Based on such computations, detailed internal kinematics of breaking waves over a slope (or over an arbitrary bottom topography) can be calculated (e.g., Grilli, Svendsen, Subramanya (1994); Grilli and Horrillo (1995)). To our knowledge, such results for breaking waves have never been obtained through numerical modeling.

## References

Brebbia, C. A. 1978: The boundary element method for engineers. John Wiley and Sons

Broeze, J. 1988: Numerical modelling of nonlinear free surface waves with a 3D panel method. Ph.D. Dissertation, Enschede, The Netherlands, 1993

Cointe, R. 1988: Remarks on the numerical treatment of the intersection point between a rigid body and a free surface. In Proc. 3rd Intl. Workshop on water waves and floating bodies. Woods Hole, Massachussets, April 1988, pp. 21–26

Cointe, R. 1990: Quelques aspects de la simulation numérique d'un canal à houle. Thèse de Doctorat de l'Ecole Nationale des Ponts et Chaussées

Cointe, R. 1990: Numerical simulation of a wave channel. Engng. Analysis with boundary elements, 7(4): 167–177

Cooker, M. J. 1990: A boundary-integral method for water wave motion over irregular bed. Engng. Analysis with boundary elements, 7(4): 205–213

Dold, J. W.; Peregrine, D. H. 1986: An efficient boundary integral method for steep unsteady water waves. In numerical methods for fluid dynamics II (ed. K. W. Morton and M. J. Baines), pp. 671–679, Clarendon Press, Oxford

Dommermuth, D. G.; Yue, D. K. P.; Lin, W. M.; Rapp, R. J.; Chan, E. S.; Melville, W. K. 1990: Deep-water plunging breakers: a comparison between potential theory and experiments. J. Fluid Mech. 189: 423–442

Gray, L. J.; Lutz, E. D. 1990: On the treatment of corners in the boundary element method. J. Comp. Appl. Math. 32: 369–386

Gray, L. J.; Manne, L. L. 1993: Hypersingular integrals at a Corner. Engng. Analysis with boundary elements 11: 327–334

Grilli, S. 1993: Modeling of nonlinear wave motion in shallow water. Chapter 3 in computational method for free and moving boundary problems in heat and fluid flow (eds. L. C. Wrobel and C. A. Brebbia), pps.37–65, Computational Mechanics Publication, Elsevier Applied Sciences, London, UK

Grilli, S.; Losada, M. A.; Martin, F. 1994: Characteristics of solitary wave breaking induced by breakwaters. J. Waterway, Port, Coastal, and Ocean Engng. 120(1): 74–92

Grilli, S.; Skourup, J.; Svendsen, I. A. 1989: An efficient boundary element method for nonlinear water waves. Engng. Analysis with boundary elements 6(2): 97–107

Grilli, S. T.; Subramanya, R. 1994: Quasi-singular integrals in the modeling of nonlinear water waves in shallow water. Engng. Analysis with Boundary Elements 13(2): 181–191

Grilli.; Horrillo, J. 1995: Exact periodic wave generation and absorption for nonlinear wave computations. J. Engng. Mech. (submitted)

Grilli, S. T.; Subramanya, R.; Svendsen, I. A.; Veeramony, J. 1994: Shoaling of solitary waves on plane beaches. J. Waterways Port Coastal Ocean Engng. 120(6): 609–628

Grilli, S.; Svendsen, I. A. 1990: Corner problems and global accuracy in the boundary element solution of nonlinear wave flows. Engng. Analysis with boundary elements, 7(4): 178–195

Grilli, S.; Svendsen, I. A.; Subramanya, R. 1994: Breaking criterion and characteristics for solitary waves on plane beaches. J. Waterway Port Coastal and Ocean Engng. (submitted)

Joo, S. W.; Schultz, W. W.; Messiter, A. F. 1990: An analysis of the initial wavemaker problem. J. Fluid Mech. 214: 161–183

Lin, W. M.; Newman, J. N.; Yue, D. K. 1984: Nonlinear forced motion of floating bodies. In Proc. 15th Intl. Symp. on Naval Hydrody., Hamburg, Germany

Longuet-Higgins, M. S.; Cokelet, E. D. 1976: The deformation of steep surface waves on water-I. A numerical method of computation. Proc. R. Soc. Lond. A350: 1–6

New, A. L.; McIver, P.; Peregrine, D. H. 1985: Computation of overturning waves. J. Fluid Mech. 150: 233–251

Otta, A. K.; Svendsen, I. A.; Grilli, S. T. 1992: Unsteady free surface waves in region of arbitrary shape. CACR, Univ. of Delaware, Res. Rept. 92-10: pp 153

Peregrine, D. H.; Breaking waves on beaches. Ann. Rev. Fluid Mech. 15: 149–178

Roberts, A. J.; Transient free-surface flows generated by a moving vertical plate, Q. J. Mech. Appl. Maths 40: 129–158

Romate, J. E. 1989: The numerical simulation of nonlinear gravity waves in three dimensions using a higher order panel method. Ph.D. Dissertation. Department of Applied Mathematics, University of Twente, The Netherland, 1989

Schultz, W. W.; Hong, S. W. 1989: Solution of potential problems using an overdetermined complex boundary integral method. J. Comp. Phys. 84: 414–440

Subramanya, R.; Grilli, S. T. 1994: Domain regridding in the computation of nonlinear waves. In Proc. 2nd Intl. Workshop on Bound. Elements in Fluid Mech. (Southampton, UK, July 1994) (eds. H. Power, C. A. Brebbia and D. B. Ingham), pps. 139–150. Comp. Mech. Publications, Elsevier Appl. Science (invited paper)

Svendsen, I. A.; Grilli, S. 1990: Nonlinear waves on steep slopes. J. Coastal Research SI7: 185–202

Svendsen, I. A.; Otta, I. A.; Grilli, S. Unsteady free surface waves. In Proc. I.U.T.A.M. Symp. on Breaking Waves (Sidney, Australia, July 91) (eds. M. L. Banner and R. H. J. Grimshaw) pp. 229–236, Springer-Verlag, Berlin

Tanaka, M. 1986: The stability of solitary waves, Phys. Fluids 29(3): 650–655

Vinje, T.; Brevig, P. 1981: Numerical simulation of breaking waves. Adv. Water Res. 4: 77–82

Wei, J.; Kirby, J. T.; Grilli, S. T. Subramanya, R. 1995: A fully nonlinear boussinesq model for surface waves. I. Highly nonlinear unsteady waves. J. Fluid Mech. 294: 71–92

Xü, H.; Yue, D. K. P. 1992: Numerical study of three dimensional overturning waves. In Proc. 7th Intl. Workshop on water waves and floating bodies. (Val de Reuil, France, May 1992) (ed. R. Cointe), Fluid Flow and Computational Aspects, pp. 303–307